INTERPLAY OF STRAIN, POLARIZATION AND MAGNETIC ORDERING IN COMPLEX OXIDES FROM FIRST PRINCIPLES

BY CARL-JOHAN EKLUND

A dissertation submitted to the

Graduate School—New Brunswick

Rutgers, The State University of New Jersey

in partial fulfillment of the requirements

for the degree of

Doctor of Philosophy

Graduate Program in Physics and Astronomy

Written under the direction of

Prof. Karin M. Rabe

and approved by

_____

_____

_____

_____

_____

New Brunswick, New Jersey

May, 2010

ABSTRACT OF THE DISSERTATION

Interplay of Strain, Polarization and Magnetic Ordering in Complex Oxides from First Principles

by Carl-Johan Eklund

Dissertation Director: Prof. Karin M. Rabe

We study mechanisms of structural and magnetic phase transitions in crystalline oxides from first principles. The focus is on epitaxial stabilization in perovskites and on magnetoelastic coupling and frustration in spinels. These materials and phenomena are of great interest for basic science and have important roles to play in the design and discovery of new functional materials.

The effects of epitaxial strain on the structure of the perovskite oxide $CaTiO_3$ are investigated. Particular attention is paid to the stabilization of a ferroelectric phase related to the polar instability found in previous first-principles studies of calcium titanate in the ideal cubic perovskite structure. At 1.5% strain, we find an epitaxial orientation transition between the *ab*-*ePbnm* phase, favoured for compressive strains, and the *c*-*ePbnm* phase. For larger tensile strains, a polar instability, which was hidden in the equilibrium bulk structure, develops in the *c*-*ePbnm* phase and an epitaxial-strain-induced ferroelectric phase is obtained with

polarization along a [110] direction with respect to the primitive perovskite lattice vectors of the square substrate. A ferroelectric rhombohedral $R3c$ phase, with a different combination of octahedral rotations, is also found to be competitive in energy for large tensile strains, and might be observable under the application of additional perturbations, such as a small degree of cation substitution.

We present an ongoing project to construct a first-principles effective Hamiltonian to investigate the transition from the high-temperature cubic phase to a low-temperature low-symmetry phase observed in the spinel structure oxides $CdCr_2O_4$ and $ZnCr_2O_4$. The local modes included in the expansion are the chromium displacements, distortions of the cadmium- or zinc-centred tetrahedra, and the homogeneous strain. The magnetostructural coupling of these degrees of freedom to the spins of the chromium ions is included in the effective Hamiltonian parametrization and first-principles determination using a symmetry analysis. The role of the magnetostructural coupling in the phase transition is analysed and discussed.

Acknowledgements

I should like to express my gratitude to my advisor, Prof. Karin M. Rabe, for her supervision and encouragement. My appreciation is also conveyed to past and present group members for providing a cordial and stimulating working environment.

Table of Contents

Chapter 1

Introduction

1.1 Background

Essential to scientific progress across many disciplines is the discovery and design of novel materials with enhanced properties. Modern experimental methods enable the synthesis and tailoring of new, potentially useful materials, and the development of a comprehensive conceptual framework for understanding their properties is of paramount interest both for fundamental science and technology. To this end, experimental investigations have traditionally constituted the primary means. Nowadays, however, alongside experimental techniques and complementing these, theoretical methods are being employed with great success. In this context so-called first-principles density-functional-theory methods, which require no assumptions based on experiments, have emerged as a powerful tool with predictive power for obtaining information on a microscopic level about the electronic and atomic structure of complex structured compounds [1, 2]. Particularly amenable to highly accurate computation within the density-functional formalism are structural properties and energetics. Largely owing to the continuing improvements in computer hardware and numerical algorithms, theory is presently used not only to interpret and explain experimental results, but also for predictions, guiding future experiments. Computations can advantage the often laborious traditional experimental trial-and-error process by screening candidate

materials, possibly as-yet unsynthesized, for desired properties. This has accelerated scientific innovation and synthesis of new complex oxide materials and heterostructures with enhanced properties as well as led to significant advances in our understanding of the fundamental physics of a wide range of systems. A recent case in point is the prediction of a strain-induced ferroelectric-ferromagnetic phase in the perovskite $EuTiO_3$ [3].

The use of density functional theory is currently limited to systems with a low or moderate degree of electronic correlation. The method is also ill-suited for finite-temperature investigations and becomes prohibitively computationally demanding for large systems (presently meaning a unit cell of around a hundred atoms). However, first-principles methods can provide a basis for the study of finite-temperature and large-scale problems when combined with other techniques. For instance, in the effective Hamiltonian approach [4–9] a symmetrized expansion in the degrees of freedom related to relevant behaviour is constructed, hence the full Hamiltonian of the system is reduced. The model Hamiltonian is fitted to first-principles calculations and used in Monte Carlo or molecular dynamics simulations to compute finite-temperature properties or to probe large systems. This and other types of first-principles modelling can develop our conceptual understanding and act as a further guide to experimentalists, especially when phenomenological investigations are impossible due to insufficient or unavailable experimental data.

The general context of this thesis is the use of first-principles methods to elucidate phenomena in complex oxides and to explore techniques the ultimate goal of which is materials-by-design. Interesting material properties often being the result of an interplay between many interacting degrees of freedom and such systems typically being difficult to probe experimentally, the atomic-scale information that first-principles can provide is especially valuable. Furthermore, from

such complexity a strong sensitivity to external fields and other perturbations can emerge, especially in the proximity of phase boundaries. The delicate phase competition may be influenced by changes in external parameters, e.g., epitaxial strain, pressure, or temperature, inducing structural phase transitions. A useful application of the first-principles method is to explore and predict structural phase boundaries by identifying low-energy alternative structures not manifested in bulk systems. The possibility of clearly distinguishing intrinsic factors from extrinsic ones facilitates assessment of their relevance and determination of the origin of observed behaviour.

Two families of crystalline oxides displaying structural motifs of sufficient complexity to exhibit many intriguing characteristics are perovskites and spinels. Materials belonging to the perovskite structure class (see Fig. 1.1) are widely studied and demonstrate virtually all of the properties found in complex oxides. The high degree of flexibility inherent in the perovskite structure renders it prone to various types of symmetry-breaking distortions—such as rotations of the oxygen tetrahedra and cation displacements—the precise details of which are crucial to the physical properties of a given compound. As a result, the perovskites exhibit a wide range of non-trivial structural phases. Their dynamics can in large part be understood in terms of soft-mode theory [10] and an often strong sensitivity of the unstable phonons to external influences such as stress can be used to drive a system through a phase transition leading to stabilization of non-bulk phases. The ease with which external factors can be incorporated within the first-principles formalism makes it highly suitable for these types of investigations.

The group of compounds crystallizing in the spinel structure (see Fig. 1.2) also exhibit a large variety of behaviours. Especially exotic phenomena are seen in the antiferromagnetic spinels whose interesting properties stem from an incompatibility between the magnetic interactions and the crystal symmetry—geometric

frustration [11]—yielding a large ground-state degeneracy which makes the systems highly sensitive towards perturbations and their behaviour notably rich and difficult to predict. In addition to a large ground-state entropy, a defining characteristic of frustrated magnets is the inability of the spins to order at temperatures of the order of the magnetic interaction. In fact, an analysis of the classical Heisenberg model for nearest-neighbour interacting spins on a lattice of vertex-sharing tetrahedra, as in the spinel structure, predicts fluctuating spins at zero temperature [12]. In a real material, all means of relieving the frustration are of course not absent; features such as further-neighbour interactions, disorder, anisotropy, and quantum effects may determinately affect the magnetic order. A particularly important mechanism for lifting the ground-state degeneracy is spin-lattice coupling which may induce a distortion of the lattice and thereby reduce the frustration and promote spin ordering. Which distinct magnetic configuration is selected under a small distortion depends ultimately on how the cost in elastic energy compares to the gain in magnetic energy.

This thesis presents first-principles investigations of spin-lattice coupling and frustration in spinels, and epitaxial stabilization [13] of novel phases at the nanoscale of perovskites. Albeit fundamental in character, these problems have tantalizing potential for technological applications and are also of direct experimental relevance. Chapter 2 treats structural phase transitions in the perovskite $CaTiO_3$. We studied the interaction between some competing structural instabilities in $CaTiO_3$ and the effect of epitaxial strain [14]. We showed that a ferroelectric phase of $CaTiO_3$ can be epitaxially stabilized—a prediction that has since been confirmed experimentally. In chapter 3 we present preliminary results addressing finite-temperature properties of two geometrically frustrated magnets, the spinels $CdCr_2O_4$ and $ZnCr_2O_4$. Both compounds have a transition to a low-symmetry structure that seems to be driven by a symmetry breaking in the spin sector

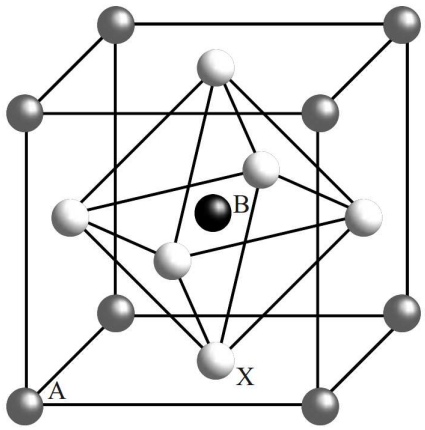

FIGURE 1.1: The ABX_3 cubic perovskite structure. The A cations are located at the cube corners, the B cations at the cube centres, and the X anions at the center of the cube faces. Alternatively, the structure can be viewed as a three-dimensional network of corner-sharing X_6 octahedra, with the A and B atoms occupying the octahedral interstices and centres, respectively. This structure belongs to the space group $Pm\overline{3}m$ and is typically the one found in the highest-temperature phase.

coupling to the lattice, as suggested by structural anomalies manifested at the magnetic phase transition. Our goal is to explore this transition by means of a first-principles effective Hamiltonian in conjunction with Monte Carlo methods to determine phase transformation thermodynamics.

1.2 Approach

We employ first-principles density-functional methods that approximately solves the many-body Schrödinger equation by variational minimization of the total energy, yielding the zero-temperature ground state for a given set of fixed atomic positions. Experience has shown that these methods give estimates of good accuracy to structural parameters and energetics for many compounds. They are less reliable in describing magnetism due to the high electronic correlation inherent in such systems, but, if used with discretion, can still provide valuable qualitative

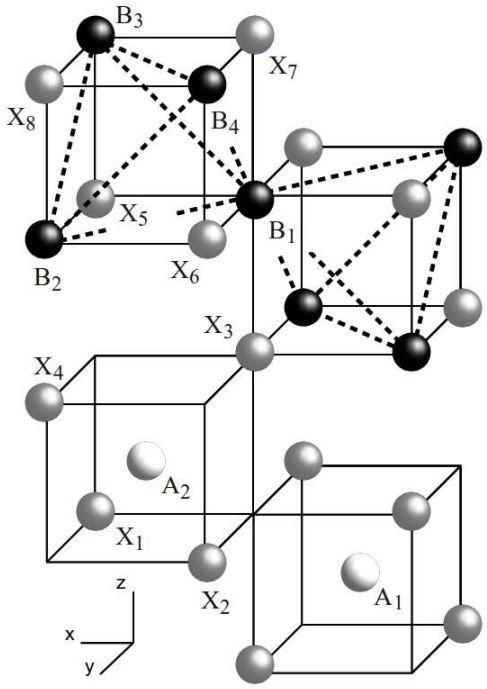

FIGURE 1.2: The AB_2X_4 cubic spinel structure [15]. It is an open structure of linked tetrahedra with the A cations occupying the centres of the X anion tetrahedra and the B cations forming a pyrochlore lattice (indicated by dashed lines). The structure belongs to the space group $Fd3m$ and has one structural parameter besides the lattice constant, viz. the anion parameter u which sets the size of the X tetrahedra. The primitive tetragonal unit cell counts two formula units, the conventional cubic cell eight. The inequivalent atoms of the primitive cell are labelled.

insight.

In this work, we frequently use total-energy calculations to survey a collection of lower-symmetry structural configurations, all of which are related to an aptly chosen higher-symmetry reference structure via moderate distortions, in order to identify low-lying phases. Each distortion introduced fixes the space group whose free structural parameters are subsequently optimized. A comparison between all structures considered allows us to determine the one with the lowest energy. All calculations are on bulk materials which are represented by means of periodic boundary conditions; a cell containing a small number of atoms is repeated to

create an effectively infinite system. Epitaxial strain is implemented by imposing appropriate epitaxial constraints on the lattice parameters of the periodic crystal (the "strained bulk" method). Information on structural stability is obtained from phonon frequencies at the zone-center and high-symmetry zone-boundary points of the Brillouin zone. The phonons are computed via the "frozen phonon" method; in this approach, a dynamical matrix is constructed from finite differences of the atomic forces resulting from small atomic displacements. We extract Heisenberg exchange constants from calculations with different collinear magnetic ordering and an otherwise unchanged structure. Other expansion parameters are determined in two ways; either through total-energy computations on sequences of distorted structures followed by polynomial fitting of the energy with respect to atomic positions and lattice parameters, or through linear combinations of force constant matrix components, computed for structures with different spin configurations and frozen-in strain.

Chapter 2

Exploring the Epitaxial Phase Diagram of Orthorhombic $CaTiO_3$

2.1 Introduction

In the extensive ABX_3 perovskite oxide family, a wide variety of equilibrium structures are observed, including ferroelectric, antiferroelectric, antiferrodistortive, and mixed-character phases. The structure of each individual phase can be described as a distortion of the ideal cubic perovskite structure (see Fig. 1.1), produced by freezing in one or more lattice instabilities of the high-symmetry cubic reference structure. This classification of perovskite structures is due to Glazer [16, 17], with a recent systematic treatment in Ref. [18]. This relation between low-symmetry phases and lattice instabilities of the cubic perovskite structure is the basis of the well-established soft-mode theory of structural phase transitions [19].

The type, strength, coupling and/or competition of instabilities are characteristic of the structural energetics of the particular compound under consideration. In the case of $CaTiO_3$, as summarized in Ref. [20], the observed equilibrium phases include a paraelectric cubic structure at high temperatures, two intermediate phases (one tetragonal and one orthorhombic), and an orthorhombic low-temperature phase with space group *Pbnm*, a structure type that includes a large number of other perovskite oxides [21]. The *Pbnm* structure is obtained by freezing in components of the M_3^+ and R_4^+ oxygen octahedron modes (notation from

Ref. [18]) involving rotation around [001] and tilting around [110], respectively, with additional changes in the lattice constants a, b and c and Ca displacements preserving the space group symmetry. Less is known about high-pressure phases, though a transition to an orthorhombic $Cmcm$ structure and, at higher pressures, to a post-perovskite structure like that of $MgSiO_3$ have been proposed based on first-principles results [22]. None of these phases are polar, though a relatively large temperature-dependent dielectric response has led to the characterization of $CaTiO_3$, like $SrTiO_3$, as an incipient ferroelectric [23].

First-principles calculations of the full phonon dispersion relation of the cubic perovskite structure of $CaTiO_3$ show that in addition to the expected instability of M_3^+ and R_4^+, the cubic perovskite structure has a third strongly unstable high-symmetry mode: Γ_4^- [21, 24, 25]. Freezing in of this polar mode, which involves displacements of the Ca and Ti ions relative to the oxygen octahedron network, would yield a ferroelectric phase with nonzero spontaneous polarization. The fact that it does not contribute to the observed bulk phases suggests that it is inhibited by the oxygen octahedron rotations; such competition has already been noted for $SrTiO_3$ where frozen-in rotational modes inhibit the polar mode [26, 27]. If the rotations are artificially suppressed, as is possible in a first-principles calculation, the Γ_4^- mode dominates and the resulting ferroelectric $P4mm$ phase is found to have a very large polarization [24, 28].

This raises the possibility that a ferroelectric phase of $CaTiO_3$ might be stabilized under conditions realizable in the laboratory. To do this, it would be necessary to change the balance of the competition between the octahedral rotations and the polar instability in favour of the latter. This can be done by strengthening the polar instability through the well-established sensitivity of the polar mode to strain in the titanates [10]. Alternatively or concurrently, the inhibition of the polar instability could be reduced by modifying the octahedral

rotation distortion. This could take the form of reducing the amplitude of the $M_3^+[001]+R_4^+[110]$ distortion in the *Pbnm* structure, or by replacing this pattern of rotations with a different pattern that allows the gain of energy associated with the strong octahedral rotation instability but that is less inhibitory to at least one polar mode component.

Both strengthening of the polar mode and modification of the octahedral distortions could be achieved though tuning epitaxial strain [29, 30]. For example, Landau theory [31] and first-principles [32, 33] analysis show that epitaxial strain on (001) substrates can change both the polar instability and the oxygen octahedron distortion patterns in $SrTiO_3$, which is paraelectric in bulk. Experimental observation of epitaxial-strain induced ferroelectricity in $SrTiO_3$ [33, 34] demonstrates this behaviour both for compressive and tensile strain.

In this work, part of which has appeared in [14], we study the use of epitaxial strain to stabilize a ferroelectric phase of $CaTiO_3$. We pursue two distinct avenues of investigation. First, we focus on the orthorhombic bulk ground state, and investigate whether epitaxial strain can induce a polar instability, analogous to the behaviour of $SrTiO_3$. The relatively low symmetry of the *Pbnm* structure requires careful attention in imposing the epitaxial constraints, and introduces new features into the strain-induced ferroelectric state. Second, we turn our attention to modifying the oxygen octahedron rotations. We perform first-principles structural optimizations to explore a large space of oxygen octahedron rotation patterns, looking for those that support a polar instability. Then, we impose the epitaxial strain constraints and compute the energies of low-lying structures. We consider epitaxial matching to square and triangular substrate lattices. In the latter case, a polar $Pmn2_1$ state remains most stable for accessible strains, although we also find a competitive rhombohedral $eR3c$ phase that might be prepared in a metastable form, or stabilized by additional perturbations such as a

small fraction of cation substitution.

Lastly, we address our discovery that the polar $Pmn2_1$ state appears for tensile, but not compressive, strains. In an unsuccessful attempt to better understand this asymmetry, we construct an energy expansion in the polar Γ_4^- mode, the rotational M_3^+ and R_4^+ modes plus two additional modes around the $Pm\overline{3}m$ structure.

2.2 Method

We performed density functional theory total-energy calculations within the local-density approximation (LDA) with projector-augmented wave potentials (PAW) [35, 36] as implemented in VASP[1] [37, 38]. The plane-wave energy cutoff was 680 eV and the Brillouin zone k-point grid was $8 \times 8 \times 8$ for the five- and ten-atom supercells and $8 \times 8 \times 6$ for the twenty-atom supercells. A grid of $6 \times 6 \times 14$ (with the dense grid in the direction of electronic polarization) was employed for the Berry phase calculations [39]. The polarization of some structures were obtained using Born effective charges [40] and atomic displacements—this is explicitly noted where applicable.

2.2.1 Structural optimizations and epitaxially strained calculations

A survey was performed of candidate ground-state and low-lying structures generated by unstable modes of the high-symmetry cubic perovskite reference structure with a computed lattice constant of 3.812 Å. The modes considered were the Γ_4^-, M_3^+, and R_4^+ modes; the ferroelectric-like mode Γ_4^- is defined by the displacement patterns of the eigenvectors with the smallest eigenvalue of the force

[1] Versions 4.6.28 and 4.6.26 of VASP were used.

constant matrix at the Γ point; the R_4^+ mode (M_3^+) corresponds to rigid rotations of the oxygen octahedra around one of their fourfold symmetry axes out of phase (in phase) in adjacent planes. This standard set of lattice modes has been extensively analysed in Ref. [18]. It generates the experimentally observed *Pbnm* ground state and allows for the possibility of ferroelectricity. While previous work has found the high-temperature cubic structure also to be unstable with respect to an X-point distortion [21], our frozen-phonon calculation yielded no unstable modes at the X-point, in agreement with Ref. [25]; the discrepancy may be due to a small difference in the lattice constant used. Since this instability is weaker, to the extent it is present at all, X-type distortions were not included in the set of modes considered for the structural optimizations. The components of our computed normalized soft-mode eigenvector of the force constant matrix at the Γ point are (Ca,Ti,$O_\perp$,$O_\perp$,$O_\parallel$)= $(0.698, 0.322, -0.440, -0.440, -0.150)$, where $O_\parallel$ and $O_\perp$, respectively, refer to motion along and transverse Ti-O bonds. The other modes are fully determined by symmetry.

The starting structures of the structural optimizations were obtained by freezing in pairs of the Γ_4^-, M_3^+, and R_4^+ modes, thereby establishing the space group symmetry of the distorted perovskite structure [18]. The minimum-energy configurations were established by relaxing the lattice parameters and the internal structural parameters until the forces on the atoms were less than 2.5 meV/Å.

For the study of the effects of epitaxial strain, we carried out "strained bulk" calculations, in which total-energy calculations are performed for the periodic crystal with appropriate epitaxial constraints imposed on the lattice parameters. In some cases, these are constraints which cannot be automatically imposed within the available VASP relaxation algorithms. In such cases, we developed an elastic energy expansion around the lowest energy *Pbnm* or *R*3*c* structure that satisfies the epitaxial constraint by fitting to the energies of structures with small changes

in strain (the latter structures not necessarily satisfying the epitaxial constraints). This energy was then minimized with respect to strain, imposing the epitaxial strain constraint; the resulting lattice parameters were then fixed in a total-energy calculation in which the internal structural parameters were relaxed.

For selected structures, we computed the stability against zone-center modes by performing frozen phonon calculations in which symmetry adapted modes or, for the *c-ePbnm* structure, single atoms were displaced by approximately 0.01 Å. From finite differences of the resulting forces, the force constant matrices were determined and subsequently diagonalized to obtain eigenfrequencies and eigenvectors.

2.2.2 Energy-surface parametrization

In an attempt to elucidate the mechanisms producing the epitaxial phase diagram, we parametrized the energy surface around the high-temperature cubic perovskite structure, hoping it would enable us to reproduce the first-principles epitaxial phase diagram and clarify the competition between the different degrees of freedom at play. The parametrization we developed is similar to that of Refs. [41, 42], but we included a larger set of modes in the expansion: Γ_4^-, R_4^+, M_3^+, X_5^+, and R_5^+ (notation from Refs. [18, 43]). The zone-boundary distortions are all present in the *Pbnm* ground state (except the component of the triply degenerate R_4^+ which describes an octahedral rotation about [001]). The Γ_4^-, R_4^+, M_3^+ have been described above. The R_5^+ involves the Ca atoms moving along $[\bar{1}10]$. The ground state $k = (0, 0, 1/2)$ X_5^+ mode consists of the Ca atoms and the O atoms at Wyckoff position 4c atoms moving along [110]; the computed components of the normalized eigenvector is (Ca, O(4c))$=(-0.912, 0.409)$. In addition to these modes, strain degrees of freedom are included in the expansion as they strongly influence the energies of the ferroelectric phases in particular. We used

the following expansion:

$$
\begin{aligned}
\Delta E = {} & \theta(R_x+R_y)MX + \theta' R_xR_y(R_x+R_y)R_5 + \tilde{\kappa}X^2 + \tilde{\alpha}X^4 + \kappa_5 R_5^2 + \alpha_5 R_5^4 \\
& + \kappa' M^2 + \alpha' M^4 + \beta' M^6 + \zeta' M^8 + \overline{\kappa}\left(R_x^2+R_y^2+R_z^2\right) + \overline{\alpha}\left(R_x^2+R_y^2+R_z^2\right)^2 \\
& + \overline{\gamma}\left(R_x^2R_y^2+R_y^2R_z^2+R_z^2R_x^2\right) + \overline{\beta}\left(R_x^2+R_y^2+R_z^2\right)^3 + \overline{\lambda}R_x^2R_y^2R_z^2 \\
& + \overline{\delta}\Big(R_x^4\left(R_y^2+R_z^2\right) + R_y^4\left(R_x^2+R_z^2\right) + R_z^4\left(R_x^2+R_y^2\right)\Big) + \overline{\zeta}\left(R_x^2+R_y^2+R_z^2\right)^4 \\
& + \overline{B}'_{xx}R_z^2M^2 + \overline{B}'_{xy}(R_x^2+R_y^2)M^2 + \overline{C}_1(R_x^2+R_y^2)X^2 + \overline{C}_2R_z^2X^2 + C'M^2X^2 \\
& + \overline{D}_1(R_x^2+R_y^2)R_5^2 + \overline{D}_2R_z^2R_5^2 + D'M^2R_5^2 + \widetilde{D}X^2R_5^2 + \frac{1}{2}\widetilde{B}_{1xx}(\eta_1+\eta_2)X^2 \\
& + \frac{1}{2}\widetilde{B}_{1yy}\eta_3X^2 + \frac{1}{2}B_1^{(5)}(\eta_1+\eta_2)R_5^2 + \frac{1}{2}B_2^{(5)}\eta_3R_5^2 + \frac{1}{2}B'_{1yy}(\eta_1+\eta_2)M^2 \\
& + \frac{1}{2}B'_{1xx}\eta_3M^2 + \frac{1}{2}\overline{B}_{1yy}\Big(\eta_1(R_y^2+R_z^2) + \eta_2(R_x^2+R_z^2) + \eta_3(R_x^2+R_y^2)\Big) \\
& + \frac{1}{2}\overline{B}_{1xx}\left(\eta_1R_x^2+\eta_2R_y^2+\eta_3R_z^2\right) + \overline{B}_{4yz}\left(\eta_4R_yR_z+\eta_5R_xR_z+\eta_6R_xR_y\right) \\
& + \frac{1}{2}B_{11}\left(\eta_1^2+\eta_2^2+\eta_3^2\right) + B_{12}\left(\eta_1\eta_2+\eta_2\eta_3+\eta_3\eta_1\right) + \frac{1}{2}B_{44}\left(\eta_4^2+\eta_5^2+\eta_6^2\right) \\
& + \kappa\left(\Gamma_x^2+\Gamma_y^2+\Gamma_z^2\right) + \alpha\left(\Gamma_x^2+\Gamma_y^2+\Gamma_z^2\right)^2 + \gamma\left(\Gamma_x^2\Gamma_y^2+\Gamma_y^2\Gamma_z^2+\Gamma_z^2\Gamma_x^2\right) \\
& + \beta\left(\Gamma_x^2+\Gamma_y^2+\Gamma_z^2\right)^3 + \delta\Big(\Gamma_x^4\left(\Gamma_y^2+\Gamma_z^2\right) + \Gamma_y^4\left(\Gamma_x^2+\Gamma_z^2\right) + \Gamma_z^4\left(\Gamma_x^2+\Gamma_y^2\right)\Big) \\
& + \lambda\Gamma_x^2\Gamma_y^2\Gamma_z^2 + C_1(\Gamma_x^2+\Gamma_y^2)X^2 + C_2\Gamma_z^2X^2 + D_1(\Gamma_x^2+\Gamma_y^2)R_5^2 + D_2\Gamma_z^2R_5^2 \\
& + B'_{xx}\Gamma_z^2M^2 + B'_{xy}(\Gamma_x^2+\Gamma_y^2)M^2 + B_{xx}\left(\Gamma_x^2R_x^2+\Gamma_y^2R_y^2+\Gamma_z^2R_z^2\right) \\
& + B_{xy}\Big(\Gamma_x^2(R_y^2+R_z^2) + \Gamma_y^2(R_x^2+R_z^2) + \Gamma_z^2(R_x^2+R_y^2)\Big) \\
& + B_{xyxy}\left(\Gamma_x\Gamma_yR_xR_y + \Gamma_y\Gamma_zR_yR_z + \Gamma_z\Gamma_xR_zR_x\right) \\
& + \frac{1}{2}B_{1yy}\Big(\eta_1(\Gamma_y^2+\Gamma_z^2) + \eta_2(\Gamma_x^2+\Gamma_z^2) + \eta_3(\Gamma_x^2+\Gamma_y^2)\Big) \\
& + \frac{1}{2}B_{1xx}\left(\eta_1\Gamma_x^2+\eta_2\Gamma_y^2+\eta_3\Gamma_z^2\right) + B_{4yz}\left(\eta_4\Gamma_y\Gamma_z+\eta_5\Gamma_x\Gamma_z+\eta_6\Gamma_x\Gamma_y\right), \qquad (2.1)
\end{aligned}
$$

where $\Delta E = E - E_0$, E_0 is the energy of the ideal cubic perovskite structure, η_i $(i = 1-6)$ are the six independent components of the strain tensor in Voigt notation, and Γ_α and R_α $(\alpha = x, y, z)$ are the Cartesian components of the soft-mode amplitudes describing the ferroelectric and antiferrodistortive mode,

respectively.

The 56 parameters appearing in the energy expansion (2.1) were determined from a series of first-principles total-energy calculations on distorted perovskite structures [41, 42]. For example, the κ', α', β', and ζ' coefficients were determined by introducing the M_3^+ distortion at different amplitudes M into the cubic perovskite structure and fitting the energy dependence on M to a polynomial of the form

$$E(M) = E_0 + \kappa' M^2 + \alpha' M^4 + \beta' M^6 + \zeta' M^8, \tag{2.2}$$

see Fig. 2.1. The coupling parameters were determined from changes in the second-order coefficients over a sequence of computations with either two modes or one mode and strain present in the system. For instance, the $\widetilde{B}_{1xx}$ coefficient was extracted from a series of total-energy computations analogous to the one just described, but with X_5^+ replacing M_3^+ and different values of η_1 frozen into the cell for each computation, see Fig. 2.2. The parameter θ (θ') was determined by comparing the energy between two structures, each of which containing a combination of R_4^+, M_3^+, and X_5^+ (R_4^+ and R_5^+) such that the product of the small amplitudes have opposite signs for the two structures.

2.3 Results

2.3.1 Structural optimizations and epitaxially strained calculations

Our results for the structure of the bulk orthorhombic ground state are given in Table 2.1. The structure has an energy 410 meV/f.u. lower than the ideal cubic perovskite structure. Consistent with previous first-principles calculations [21, 25], we find good agreement between the computed structure and experiment,

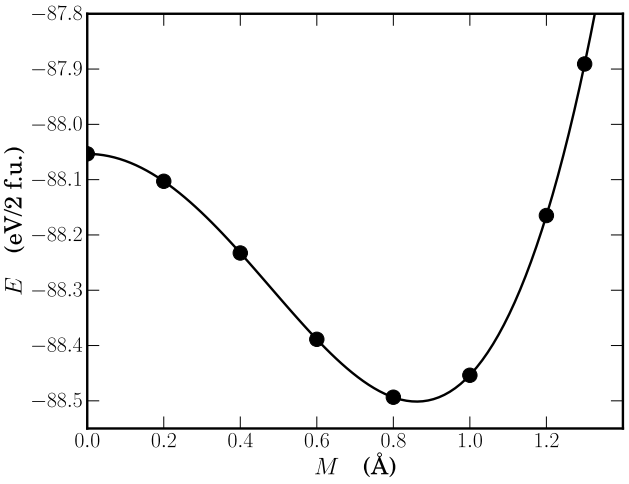

FIGURE 2.1: Depicts the energy as a function of M_3^+ amplitude. The fit (solid line) was used to determine the interaction parameters in Eq. 2.2.

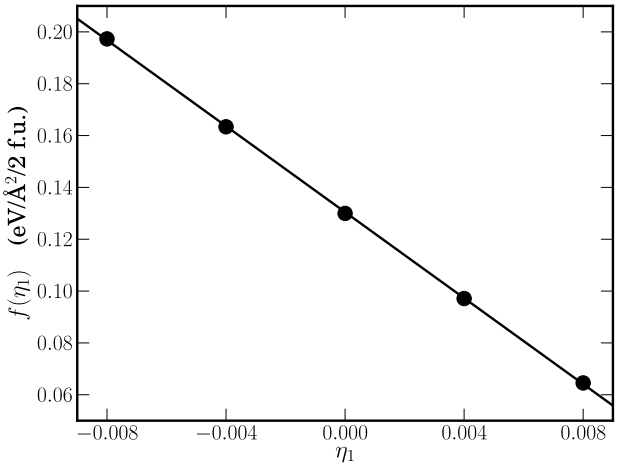

FIGURE 2.2: Shows $f(\eta_1) = \tilde{\kappa} + \frac{1}{2}\widetilde{B}_{1xx}\eta_1$. The slope reflects the coupling coefficient between X_5^+ and η_1.

TABLE 2.1: The Wyckoff parameters of the *Pbnm* ground state and the *c*-*ePbnm* structure at 4% tensile strain.

	Pbnm	*c*-*ePbnm*
Ca (4c)	$x = 0.510, y = -0.047$	$x = 0.509, y = -0.042$
Ti (4a)	–	–
O (4c)	$x = 0.081, y = 0.021$	$x = 0.085, y = 0.022$
O (8d)	$x = 0.207, y = 0.292,$ $z = -0.043$	$x = 0.218, y = 0.283,$ $z = -0.044$

taking into account that in the local density approximation lattice constants typically tend to be underestimated by about one percent.

Next, we investigated the effects of epitaxial strain on the *Pbnm* phase. As in Ref. [44], we designated the strained phases as *ePbnm*, where the prefix *e* denotes "epitaxial." We first considered epitaxial strain on a square lattice substrate, corresponding to a (001) perovskite surface. To allow direct comparison with experiment despite the lattice constant underestimate discussed above, we defined epitaxial strain relative to $a_0 = 3.77$ Å, which is the cube root of the computed volume per formula unit of the relaxed *Pbnm* structure. In the *Pbnm* structure, there are two symmetry-inequivalent primitive perovskite (001) planes, as shown in Fig. 2.3. Thus, there are two distinct orientations for an epitaxial film: the first, with *c* in the substrate plane and *a* and *b* out of the plane (*ab*-*ePbnm*, Fig. 2.3 (a)), and the second, with *c* normal to the matching plane (*c*-*ePbnm*, Fig. 2.3(b)).

We computed the total energies for these two orientations for epitaxial strains ranging from −1.5% to 4% [2]. For *c*-*ePbnm*, the *c* lattice parameter and internal

[2]The strain values are −1.51%, −1.01%, 1.01%, 2.02%, 3.03%, and 4.05%.

structural parameters were relaxed at each strain, maintaining the $Pbnm$ symmetry; the a and b lattice parameters are fixed by the constraint to equal $\sqrt{2}a_s$, where a_s is the side of the square substrate. The epitaxial constraint allows for $\boldsymbol{t}_c$ not to be normal to the matching ab-plane and tilting $\boldsymbol{t}_c$ could lower the energy. However, an elastic analysis for the -1.5% and 4% cases showed that tilting $\boldsymbol{t}_c$ does not lower the energy and we assumed this to be true for the intermediate strains as well. ab-$ePbnm$ has lower symmetry than c-$ePbnm$; that is, distinguishing one of the two (110) planes removes space group symmetries, resulting in a space group $P2_1/m$; the constraint fixes

$$|\boldsymbol{t}_c| = 2a_s \text{ and } |\boldsymbol{t}_b - \boldsymbol{t}_a| = 2a_s, \tag{2.3}$$

as well as the condition

$$\boldsymbol{t}_c \cdot (\boldsymbol{t}_b - \boldsymbol{t}_a) = 0. \tag{2.4}$$

To optimize the lattice parameters for this case, we used the elastic energy expansion method described in Sec. 2.2.1.

The results are shown in Fig. 2.4. ab-$ePbnm$ is favourable for compressive strains and c-$ePbnm$ is favourable for tensile strains. Within this subspace of nonpolar structures, there is an epitaxial orientation transition at 1.5 %.

Next, we turned to the stability of the $ePbnm$ phases against symmetry-breaking distortions, with special attention to polar phonons. Previous computation of the phonon frequencies for the bulk equilibrium structure showed three low-frequency polar phonons at 94 cm^{-1}, 88 cm^{-1} and 89 cm^{-1}, with induced polarizations along a, b and c, respectively [25]. These phonons are expected to be sensitive to changes in strain, based on known polarization-strain coupling in calcium titanate [42].

We first considered c-$ePbnm$ with 4% tensile strain, with computed structural

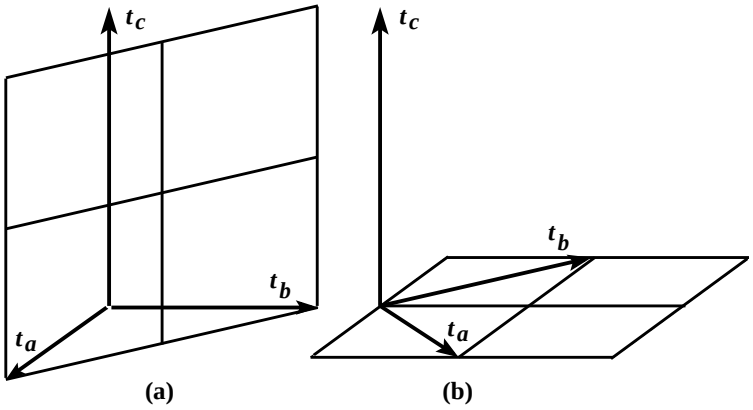

FIGURE 2.3: The two distinct relative orientations of the lattice vectors and the primitive perovskite substrate matching planes in the *Pbnm* structure are shown for (a) the *ab-ePbnm* phase and (b) the *c-ePbnm* phase.

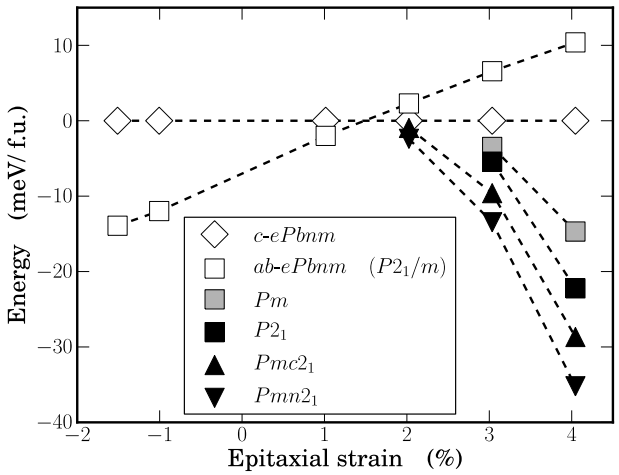

FIGURE 2.4: Total energy per five-atom formula unit for various epitaxially constrained structures as a function of square misfit strain. At each strain, the energy of the *c-ePbnm* structure is taken as the zero of energy. The symbols show the result of the calculations, the lines are merely a guide to the eye.

parameters reported in Table 2.1. A zone-center frozen phonon computation for this structure showed four unstable phonons, the lowest two, at 213i cm^{-1} and 209i cm^{-1}, being polar and generating structures with space groups $Pmn2_1$ (polarization along a) and $Pmc2_1$ (polarization along b), respectively. In both cases, the orientation of polarization with respect to the primitive perovskite axes is along the [110] directions. The energies of the structures for these two space groups, optimized under the epitaxial strain constraint, are 35 meV/f.u. and 28 meV/f.u. below *c*-*ePbnm*, respectively, with polarizations 46 $\mu C/cm^2$ and 45 $\mu C/cm^2$ computed using Born effective charges and atomic displacements [40]. Thus, at 4% tensile strain, we predict strain-induced ferroelectricity in $CaTiO_3$.

For the full range of strains, the unconstrained internal structural parameters were optimized within these two polar space groups. Only in the 4% case were $|\boldsymbol{t}_c|$ re-optimized for the polar structures as this only had a marginal effect on the energy and the polarization compared to when the relaxed value for the *c*-*ePbnm* structure was used, presumably because the polarizations are in the *ab*-plane. At compressive strain, the nonpolar *c*-*ePbnm* structure is stable against polar distortions, and no ferroelectricity is observed. For tensile strain, the ferroelectric instabilities first appear at 2% strain, and the energy gain and polarization of the optimized ferroelectric phases grow with increasing strain.

Let us now consider *ab*-*ePbnm* with 4% tensile strain. We looked for polar instabilities in this structure by displacing atoms in such a way that the resulting, lowered symmetry allowed for nonzero polarization, and then relaxing the internal structural parameters while keeping the lattice parameters fixed at their *ab*-*ePbnm* values. This procedure revealed two structures with polarizations in the matching plane of 33 $\mu C/cm^2$ along c (space group $P2_1$) and 40 $\mu C/cm^2$ along the ab diagonal (space group Pm), respectively. (The polarizations were obtained using Born effective charges and atomic positions [40].) The former is

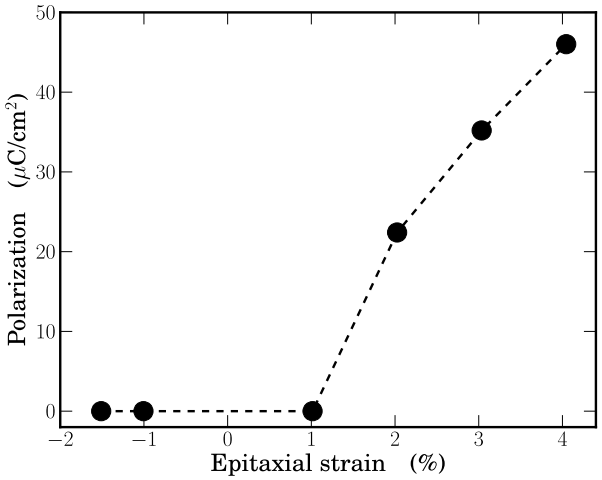

FIGURE 2.5: Shows the magnitude of the polarization of the lowest-energy structure in Fig. 2.4 for each value of epitaxial strain.

the lowest in energy but still above $Pmn2_1$ and $Pmc2_1$, see Fig. 2.4. This procedure was also carried out for epitaxial strains of 3% and −1.5%. No polar phase was found in the latter case. Fig. 2.5 shows the magnitude of the polarization of the lowest-lying structure at each value of epitaxial strain imposed by square substrate.

For both epitaxial orientations, we decomposed the structures at each strain into the R_4^+, M_3^+, X_5^+, and R_5^+ modes (the atomic displacement ratios of the X_5^+ mode were those of the ground state) by projecting the atomic positions onto the space spanned by this set of distortions. The result is presented in Figs. 2.6 and 2.7. For comparison, the corresponding ground state amplitudes are: (R_4^+, M_3^+, X_5^+, R_5^+)= $(0.167, 0.170, 0.102, 0.020)$.

Next, we investigated the possibility of a transformation as a function of strain to another structure type. If such a transformation fails to occur, it would strengthen our prediction for the observation of strain-induced ferroelectricity in *Pbnm*; if it were to occur, the identification of a new phase and phase boundary

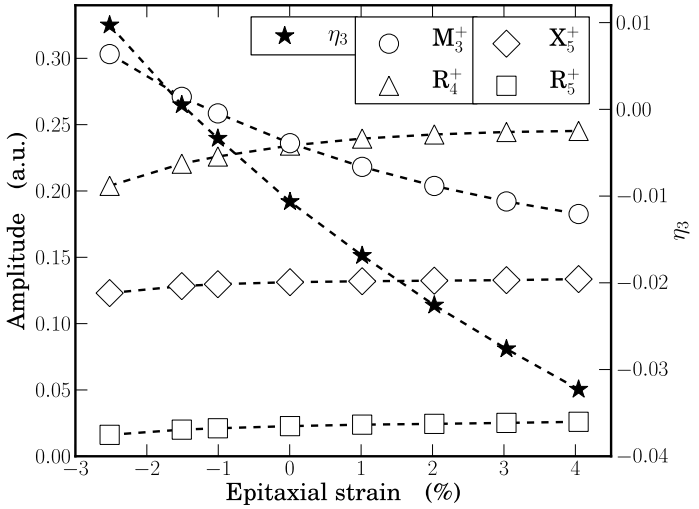

FIGURE 2.6: Mode decomposition in relative arbitrary units and η_3 of the *c-ePbnm* structure at various square misfit strains. The X_5^+ atomic displacement ratios are those of the ground state. The strain values are -2.52%, -1.51%, -1.01%, 0.00%, 1.01%, 2.02%, 3.03%, and 4.05%.

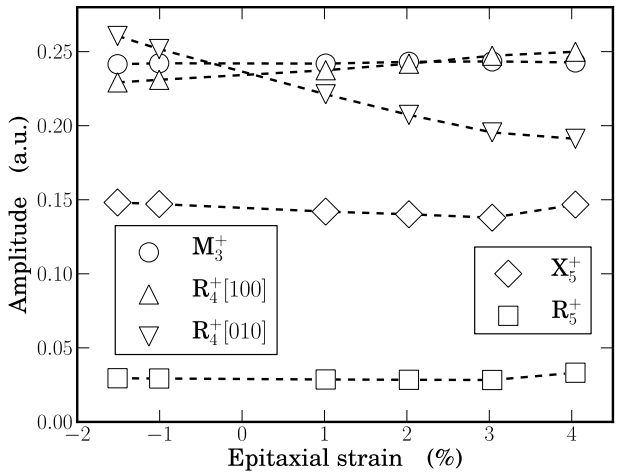

FIGURE 2.7: Mode decomposition of the *ab-ePbnm* structure in relative arbitrary units at various square misfit strains. The R_4^+ directions are with respect to the cubic perovskite axes.

would be of great interest in the functional behaviour of $CaTiO_3$.

We considered a range of structures obtained by freezing in Γ_4^-, M_3^+, and R_4^+ modes and relaxing the structure within the resulting space group. The computed energies of the structures considered are summarized in Table 2.2; the equilibrium lattice parameters for each structure are given in Table 2.3. The data show that in the space of structures defined by the distortions Γ_4^-, M_3^+, and R_4^+, the R_4^+ instability is the dominant one. When separately introduced into the system, the R_4^+ mode leads to structures that are the lowest in energy, the M_3^+ yields structures a fair amount higher in energy, and the Γ_4^- distortion leads to much higher-lying structures. The instability of the cubic high-energy structure (space group $Pm\overline{3}m$) with respect to the polar Γ_4^- mode is, however, clearly evident.

The situation is different when we introduce combinations of the Γ_4^- mode and the M_3^+ or R_4^+ mode into the system. The polar mode is consistently suppressed by the rotational modes, a phenomenon touched upon in the introduction. In some cases the polar instability is completely eliminated, e.g. $\Gamma_4^-[001]$ combined with $R_4^+[001]$, $R_4^+[110]$, or $M_3^+[001]$. However, certain combinations of modes allow the polar character to partly remain; a key observation to make from the data in Table 2.2 is that a polar phase with both the ferroelectric Γ_4^- distortion and the antiferrodistortive R_4^+ distortion frozen in along the [111] direction lies at only about 70 meV per formula unit above the *Pbnm* ground state. This polar structure has the trigonal space group $R3c$, hence representing a different class of structures than the orthorhombic ground state and non-polar phase obtained by relaxing $R_4^+[110]$ (which is close in energy to the $R3c$ phase). The computed spontaneous polarization, 45 $\mu C/cm^2$ along the [111] direction, is quite large, being, for example, almost twice the spontaneous polarization of the prototypical ferroelectric $BaTiO_3$ [19].

One needs to keep in mind that it cannot be concluded from the structural

TABLE 2.2: Energy in meV per formula unit relative to the perfect cubic perovskite structure of various structures obtained from the first-principles structural optimizations (in decreasing order). The choices of axes follow the conventions of Table 1 in Ref. [18]. Also listed are the polarizations in μC/cm^2 of the polar structures computed via the Berry phase technique [39]. Brackets signify that the optimized structure belongs to the space group of highest symmetry.

$\Gamma_4^-[111]$	-40	53	$R3m$
$\Gamma_4^-[001]$	-70	69	$P4mm$
$\left.\begin{matrix}\mathrm{M}_3^+[001] \\ \mathrm{M}_3^+[001]+\Gamma_4^-[001]\end{matrix}\right\}$	-260		$\left\{\begin{matrix}P4/mbm \\ P4bm\end{matrix}\right.$
$\mathrm{M}_3^+[100]+\Gamma_4^-[001]$	-270	32	$Amm2$
$\mathrm{M}_3^+[001]+\Gamma_4^-[110]$	-270	38	$Pmc2_1$
$\left.\begin{matrix}\mathrm{R}_4^+[001] \\ \mathrm{R}_4^+[001]+\Gamma_4^-[001]\end{matrix}\right\}$	-300		$\left\{\begin{matrix}I4/mcm \\ I4cm\end{matrix}\right.$
$\mathrm{R}_4^+[111]$	-320		$R\overline{3}c$
$\mathrm{R}_4^+[111]+\Gamma_4^-[111]$	-340	45	$R3c$
$\left.\begin{matrix}\mathrm{R}_4^+[011] \\ \mathrm{R}_4^+[110]+\Gamma_4^-[001] \\ \mathrm{R}_4^+[110]+\Gamma_4^-[110]\end{matrix}\right\}$	-340		$\left\{\begin{matrix}Imma \\ Ima2 \\ Ima2\end{matrix}\right.$
$\left.\begin{matrix}\mathrm{M}_3^+[001]+\mathrm{R}_4^+[110] \\ \mathrm{M}_3^+[001]+\mathrm{R}_4^+[110]+\Gamma_4^-[001] \\ \mathrm{M}_3^+[001]+\mathrm{R}_4^+[110]+\Gamma_4^-[\overline{1}10] \\ \mathrm{M}_3^+[001]+\mathrm{R}_4^+[110]+\Gamma_4^-[110]\end{matrix}\right\}$	-410		$\left\{\begin{matrix}Pbnm \\ Pna2_1 \\ Pmn2_1 \\ Pmc2_1\end{matrix}\right.$

TABLE 2.3: Computed lattice parameters in Ångström and degrees for the structures in Table 2.2.

$R3m$	$a = 3.82$, $\phi = 89.4$
$P4mm$	$a = 3.78$, $c = 3.94$
$P4/mbm$	$a = 5.29$, $c = 3.86$
$Amm2$	$a = 3.85$, $b = 7.48$, $c = 7.54$
$Pmc2_1$	$a = 3.84$, $b = 5.32$, $c = 5.33$
$I4/mcm$	$a = 5.29$, $c = 7.71$
$R\bar{3}c$	$a = 5.33$, $\phi = 60.6$
$R3c$	$a = 5.36$, $\phi = 60.0$
$Imma$	$a = 5.36$, $b = 7.51$, $c = 5.38$
$Pbnm$	$a = 5.29$, $b = 5.40$, $c = 7.53$

optimization that the $R3c$ phase is a local minimum. It is not a tractable task to compute full phonon dispersions using VASP; therefore, in order to obtain at least some information about the stability of the $R3c$ structure, we performed frozen-phonon computations at the Γ, L, and X points (the lattice was approximated to be face-centred cubic during the symmetry analysis of the zone-boundary phonons). No unstable phonons were found; the lowest-frequency phonons were at 85 cm^{-1}, 97 cm^{-1}, and 108 cm^{-1} at the Γ, L, and X point, respectively. Although this result does not prove that the $R3c$ phase is a local minimum, we found it encouraging enough to warrant an investigation of the effects of epitaxial strain on the $R3c$ phase.

First, we considered epitaxial strain on a square substrate surface with the strain measured relative to $a_0 = 3.77$ Å (the cube root of the computed volume per formula unit of the relaxed $Pbnm$ structure). The lattice parameters were optimized by means of the elastic energy expansion method described in Sec. 2.2.1. The space group of the optimized structures is Cc [45] and they are denoted by $eR3c$. As can be seen in Fig. 2.8, the resulting structure is 24 meV/f.u.

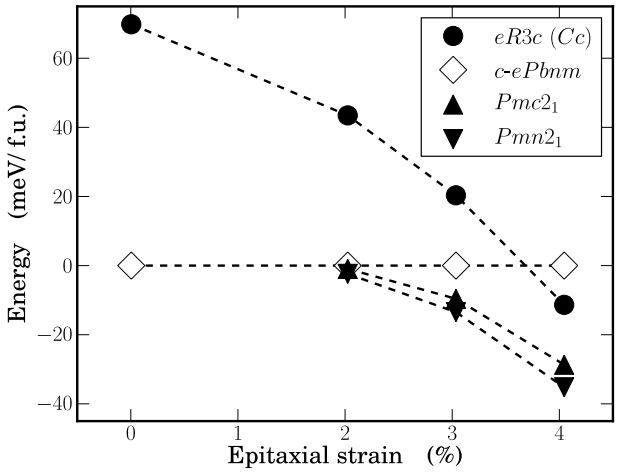

FIGURE 2.8: Total energy of the $eR3c$ phase on a square substrate is plotted with solid circles for comparison with the energies of nonpolar c-$ePbnm$ (taken as the zero of energy at each strain and shown as open diamonds) and the two polar phases $Pmn2_1$ and $Pmc2_1$ (solid triangles). The connecting lines are a guide to the eye.

above the polar $Pmn2_1$ phase at 4% strain, but below nonpolar c-$ePbnm$. Using Born effective charges [40] and atomic positions, the polarization comes out to be 75 μC/cm^2 and has both in- and out-of-plane components. Extrapolation of the curves for the polar $ePbnm$ phases and for $eR3c$ suggests that the latter might become more stable for higher strains, but these would be too large to be experimentally accessible.

Lastly, we explored the idea that matching the structures to a triangular substrate surface might favour a rhombohedral structure such as the $R3c$ relative to an orthorhombic one like the $Pbnm$ ground state. There are two distinct primitive perovskite (111) planes in the $Pbnm$ structure, see Fig. 2.9. Consequently, the matching of the $Pbnm$ structure to a triangular substrate with side $l \approx \sqrt{2}a_0$ (where a_0 is the primitive perovskite constant) can be implemented via either of

the following two constraints:

$$|\boldsymbol{t}_a + \boldsymbol{t}_b - \boldsymbol{t}_c| = |-\boldsymbol{t}_a + \boldsymbol{t}_b - \boldsymbol{t}_c| = 2l, \text{ and } |\boldsymbol{t}_a| = l, \tag{2.5}$$

or

$$|\boldsymbol{t}_a + \boldsymbol{t}_b - \boldsymbol{t}_c| = |\boldsymbol{t}_a - \boldsymbol{t}_b - \boldsymbol{t}_c| = 2l, \text{ and } |\boldsymbol{t}_b| = l. \tag{2.6}$$

Similarly, the lattice vectors of the $R3c$ structure must satisfy the following relation:

$$|\boldsymbol{t}_i + \boldsymbol{t}_j| = l, \tag{2.7}$$

where $i, j = 1, 2, 3$. The constraint (2.7) has one free parameter.

We performed constrained structural optimizations for strains ranging from -0.5% to 3.5% [3]. As before, the strain is defined relative to $a_0 = 3.77$ Å, the cube root of the computed volume per formula unit of the relaxed $Pbnm$ structure. The $eR3c$ structure was optimized with respect to constraint (2.7) by first finding the optimal lattice vectors through a sequence of total-energy computations and then relaxing the internal parameters while keeping the optimal lattice parameters fixed. The $ePbnm$ structure was optimized using the energy expansion method described in Sec. 2.2.1, resulting in structures having the symmetry $P2_1/c$.

The relative energies of the optimized structures are shown in Fig. 2.10. The non-polar $P2_1/c$ structure remains lower than $eR3c$ at all values of epitaxial strain; in fact, the energy difference between the two structures does not change significantly with strain. The naïve idea that epitaxial matching to a triangular lattice would energetically favour the rhombohedral $R3c$ structure over the orthorhombic $Pbnm$ therefore proved incorrect. Interestingly, we do, as we did when using a square substrate, observe an orientational transition. This is seen

[3] The strain values are -0.55%, 0.45%, 1.46%, 2.46%, and 3.47%

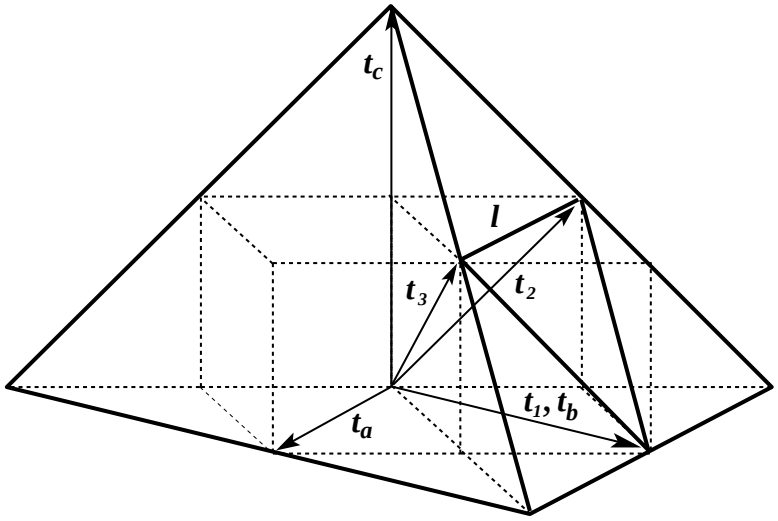

FIGURE 2.9: A schematic depiction of the $eR3c$ and $ePbnm$ structures when matched to a triangular substrate. The one (two) distinct orientation(s) of the triangular substrate plane relative to the $R3c$ ($Pbnm$) lattice vectors are shown.

in the $ePbnm$ data in Fig. 2.10, which is included for this purpose (note that the constraints (2.5) and (2.6) can be satisfied without breaking the $Pbnm$ symmetry). Below 0.5%, the structure with $\boldsymbol{t}_a$ in the epitaxial plane (which satisfies (2.5)) is lower in energy than the structure with $\boldsymbol{t}_b$ in the epitaxial plane (which satisfies (2.6)). Above 0.5%, the roles are reversed. There is a corresponding orientational transition of the $P2_1/c$ structure.

For the largest tensile strain considered, a frozen-phonon computation showed that there were no unstable zone-center phonons in the $eR3c$ structure, although the lowest frequency had decreased relative to that of the unstrained $R3c$ structure (from 85 cm^{-1} to 58 cm^{-1}).

2.3.2 Energy-surface parametrization

The energy expansion (2.1) failed to adequately describe the structural energetics of the subspace defined by the Γ_4^-, R_4^+, M_3^+, X_5^+, and R_5^+ distortions. The

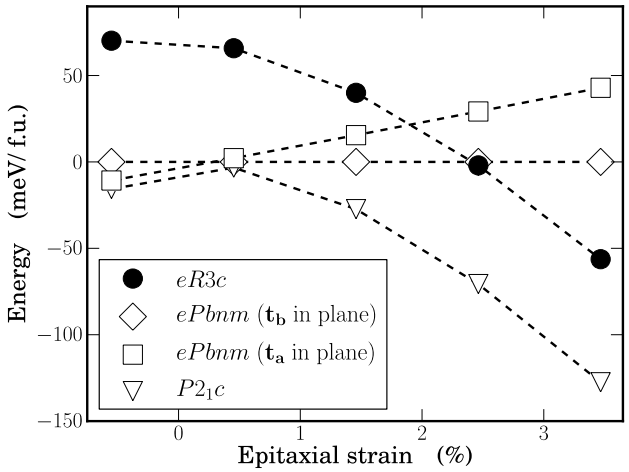

FIGURE 2.10: Total energy per five-atom formula unit for various epitaxially constrained structures as a function of triangular misfit strain. At each strain, the energy of the *ePbnm* structure satisfying constraint (2.5) is taken as the zero of energy. The lines are a guide to the eye.

coefficients obtained through the procedure outlined in Sec. 2.2.2 are listed in Table 2.4.

2.4 Discussion

2.4.1 Structural optimizations and epitaxially strained calculations

The mechanism of strain-induced ferroelectricity in the *Pbnm* phase is closely related to that for $SrTiO_3$, which similarly has a high strain sensitivity of the low-frequency polar mode. However, the effect in $SrTiO_3$ is equally strong for compressive as for tensile strain, as elongation of the unit cell produced by compressive strain destabilizes the polar mode as effectively as elongation in the in-plane direction for tensile strain. This is a direct consequence of the fact that $SrTiO_3$ is cubic in the paraelectric phase; the octahedron transition being at low

TABLE 2.4: The first-principles coefficients of the energy expansion (2.1). The units are such that the energy is in eV/f.u. given mode amplitudes in Å. The modes are normalized so that the square root of the sum of the squared atomic displacements of a ten-atom cell equals 1 Å (except Γ_x, Γ_y, and Γ_z which are analogously normalized with respect to the five-atom cell).

κ	-0.90	α'	0.51	B_{xx}	3.86	$\overline{B}_{4yz}$	0.43
α	8.65	β'	-0.08	B_{xy}	1.97	$\widetilde{B}_{1yy}$	-4.07
γ	-3.60	ζ'	0.01	B_{xyxy}	-5.92	$\widetilde{B}_{1xx}$	-8.29
β	-9.65	$\tilde{\kappa}$	0.06	B_{1xx}	-51.69	$B_1^{(5)}$	-8.99
δ	16.09	$\tilde{\alpha}$	1.30	B_{1yy}	8.93	$B_2^{(5)}$	-4.79
λ	11.97	κ_5	0.64	B_{4yz}	-9.74	B_{11}	139.42
$\overline{\kappa}$	-0.71	α_5	0.65	B'_{xx}	3.63	B_{12}	37.00
$\overline{\alpha}$	0.54	θ	-0.45	B'_{xy}	1.27	B_{44}	34.55
$\overline{\gamma}$	-0.25	θ'	-0.65	B'_{1xx}	≈ 0	D_1	4.37
$\overline{\beta}$	-0.09	C_1	10.76	B'_{1yy}	6.67	D_2	3.52
$\overline{\delta}$	0.16	C_2	3.16	$\overline{B}'_{xx}$	2.66	$\overline{D}_1$	0.91
$\overline{\lambda}$	0.31	C'	0.40	$\overline{B}'_{xy}$	0.73	$\overline{D}_2$	0.73
$\overline{\zeta}$	0.01	$\overline{C}_1$	1.47	$\overline{B}_{1xx}$	1.45	D'	0.47
κ'	-0.64	$\overline{C}_2$	0.61	$\overline{B}_{1yy}$	6.81	$\widetilde{D}$	≈ 0

temperatures and the rotational distortion not being strong enough to inhibit the strain-enhanced polar instability.

In $CaTiO_3$, in contrast, the rotational instabilities are much stronger and the resulting distortions are much larger. No ferroelectric *ePbnm* phase was found for compressive strain, despite elongation of the unit cell along the direction normal to the surface; this presumably is due to inhibition by the pattern of octahedral rotations. This highlights the idea that in a nonpolar low-symmetry phase, unlike in a cubic phase, the relationship between the crystal axes and the epitaxial constraints is very important, different choices yielding quite distinct structures and coupling to potential instabilities.

To investigate the relative importance of enhancing the polar instability compared to suppressing the rotational instabilities, we analysed the structural parameters of the *c-ePbnm* and *ab-ePbnm* phases as a function of epitaxial strain. Figs. 2.6 and 2.7 display a tendency for one rotational mode to weaken with increasing strain, albeit the rotational amplitudes remain large throughout the entire range of strains reported here, suggesting that the dominant mechanism of the strain-induced ferroelectricity is the strain enhancement of the polar instability. Indeed, the rotational instabilities are so strong that it is unlikely that they can be suppressed by epitaxial constraint alone, though it is possible that appropriate epitaxial strain could favour a combination of rotations that was less inhibitory to a polar instability, at least along some direction, as we have found in the *R*3*c* structure. A different avenue to suppress rotations has been proposed: that of isoelectronic substitution of some of the Ca with larger ions [46]. Because of the long coherence length of the octahedral rotations, resulting from the sharing of oxygen atoms between octahedra, this local change could suppress the rotations over a much longer length scale and thus have effects for a relatively small degree of substitution.

In comparing these predictions with experiments on epitaxial strained $CaTiO_3$, it is important to keep in mind that our approach considers only the effect of strain on the ground state structure and properties. In a real thin film, especially the ultrathin films needed to sustain very high strains, other factors can affect the observed phase, including temperature, the atomic arrangements at the substrate and the film-substrate interface, relaxation, reconstruction, and adsorption at the free surface, and defects and impurities in the film itself. However, the tendency to ferroelectricity with increasing tensile strain is clear in our results, and to the extent that these other factors do not act dominantly against it, we expect ferroelectricity in $CaTiO_3$ to be observed at experimentally accessible strains.

2.4.2 Energy-surface parametrization

As noted in Sec. 2.3.2, the predictions of the energy expansion (2.1) are not in qualitative agreement with the first-principles results. The most significant cause for disagreement between the two methods is probably due to the interactions being included only to the lowest order. This approximation limits the expansions applicability given the large distortions present in the $CaTiO_3$ and the large strains being sampled. Another source of error is that the atomic displacement ratios of the Γ_4^- and X_5^+ modes are fixed in the computations and may not agree particularly well with the optimized atomic displacements.

Chapter 3

Phase Transitions and Magnetostructural Coupling in $CdCr_2O_4$ and $ZnCr_2O_4$

3.1 Introduction

Magnetic and structural frustration promotes the development of exotic magnetic orderings unobserved in non-frustrated systems and presents a formidable challenge to theorists and experimentalists alike. The inherent complexity of the physics of frustration renders complementary theoretical and experimental investigations crucial for improving our understanding of systems exhibiting this phenomenon. In this spirit, first-principles computations can provide valuable quantitative predictions about the structural and magnetic energetics, phases, and phase boundaries, facilitating interpretation and explanation of experimental results and providing useful information for future experimental investigations.

In this chapter, we address finite-temperature properties of a particular class of geometrically frustrated antiferromagnets by applying a first-principles effective Hamiltonian approach to the spinels $CdCr_2O_4$ and $ZnCr_2O_4$. Spinels and pyrochlores are prototype systems for geometrical frustration. The effect is especially striking in $CdCr_2O_4$ and $ZnCr_2O_4$ so these materials lend themselves well for the study of frustration. Moreover, their chemical and structural similarities, yet manifestly dissimilar ground states, offer opportunity for comparison and investigation of the multiple ways to relieve frustration compatible with the spinel structure.

$CdCr_2O_4$ and $ZnCr_2O_4$ belong to a family of binary chalcogenides with the chemical formula AB_2X_4, where A and B are cations and X is an anion, and which crystallize over a wide temperature range in the cubic spinel structure [15]. One representation of the structure is illustrated in Fig. 1.2. A salient feature is its incompatibility with the antiferromagnetic interaction between the magnetic Cr^{3+} ions ($S = 3/2$). More precisely, the magnetic moments form a network of vertex-linked tetrahedra—a pyrochlore lattice [47]—and when magnetic moments preferring anti-alignment reside on such a lattice, all interactions cannot be satisfied simultaneously, resulting in frustration [48]. Experimentally, the large amount of low-energy entropy is evidenced by the spins failing to order at the temperature expected from the Curie-Weiss constant which is a measure of the characteristic strength of the interaction between the magnetic moments. For $ZnCr_2O_4$, the Curie-Weiss temperature is 390 K whereas the spins order at the much lower Néel temperature of 12.5 K after a spin-driven effect has introduced a distortion of the lattice, thereby lowering the symmetry and relieving the geometric frustration in the process. Also $CdCr_2O_4$ enters a spin-ordered state, the Néel and Curie-Weiss temperatures are 7.8 K and 88 K, respectively. The structural anomalies observed at the magnetic transitions strongly indicate that the coupling between spin and lattice degrees of freedom plays a major role in these first-order transitions from the paramagnetic cubic state to the antiferromagnetic states. Much regarding the details of the latter phases remain unclear, e.g. their precise spin structure. Like many frustrated compounds, however, $CdCr_2O_4$ and $ZnCr_2O_4$ form complicated non-collinear spin structures as a way to relieve the frustration. The spatial orientation of the magnetic moments have been examined via neutron diffraction using both single-crystal and powder samples (only $ZnCr_2O_4$). The low-symmetry state of $ZnCr_2O_4$ has a complex commensurate magnetic order with coplanar spins in the [110] plane, the exact details of which

has yet to be resolved [49–51]. The measurements suggest that $ZnCr_2O_4$ is proximate to several spin configurations after the transition from the high-symmetry cubic phase to the low-temperature low-symmetry state. $CdCr_2O_4$, in contrast, has a somewhat better understood incommensurate spin structure with a characteristic wave vector of $\mathbf{Q}_M = (0, d, 1)$, where $d \approx 0.09$, with the spins lying in the [101] plane [49, 52]. A major complication in these experiments are the small structural distortions of the magnetically ordered phases relative to the cubic paramagnetic phases, making it challenging to distinguish between different crystal domains. The distortions have been measured with single-crystal X-ray diffraction. For $ZnCr_2O_4$, the low-temperature low-symmetry state is reported as tetragonal $I\overline{4}m2$ [49, 50] or orthorhombic $F222$ [53] (motivated by results from a single-crystal electron-spin-resonance study). The lattice distortion of the low-symmetry structure of $CdCr_2O_4$ is distinctly different from that of $ZnCr_2O_4$, involving a simple elongation of the c-axis as opposed to a contraction for $ZnCr_2O_4$ the transition of which also involves additional local distortions. The space group of the low-symmetry phase of $CdCr_2O_4$ is tetragonal $I4_1/amd$ [49].

Magnetostructural coupling in $CdCr_2O_4$ and $ZnCr_2O_4$ have been studied from first-principles calculations [54–56]. The focus has been on how the symmetry breaking in the spin sector is manifested in the energetics of the structure. In short, one has computed the splittings induced by antiferromagnetic ordering on the infrared active phonon modes. The calculations show that a cubic-to-tetragonal symmetry lowering, induced by changing the magnetic order from ferro- to antiferromagnetic while keeping the crystal fixed, produces a significant splitting in frequency among the infrared active phonons (which are degenerate in the cubic case). This magnetically induced phonon anisotropy demonstrates a coupling between the magnetic order and the lattice.

The collinear spin arrangement used in the first-principles computations represents a simplification of the true spin structures. We intend to study these materials more systematically by means of an effective Hamiltonian. This is an approximate interpolative method which has proved capable of explaining the effects of temperature when combined with the intrinsically zero-temperature first-principles scheme. It has been successfully applied to, e.g., several perovskite compounds [4–7], including more recently multiferroic $BiFeO_3$ [8, 9] in which spontaneous magnetism and polarization coexist and are strongly coupled. Our main focus is to elucidate the interplay between the magnetic and structural degrees of freedom in these spinels, a mechanism which plays an important role in other classes of compounds as well, e.g., multiferroics. We thereby hope to contribute to the interpretation of the experimental data and help resolve the issues regarding the magnetic order in both materials and the ground state of $ZnCr_2O_4$. We would also like to enhance our general understanding of the different ways frustration is relieved in spinels. This is a work in progress, we will present the part that is finished and a brief outline of what remains.

3.2 Method

Our goal is to construct an effective Hamiltonian to investigate the phase transitions in the geometrically frustrated spinels $CdCr_2O_4$ and $ZnCr_2O_4$. This computationally advantageous approach rests on the assumption that the energetics of system under study can be adequately modelled by a Taylor expansion around a high-symmetry structure using only a restricted set of judiciously chosen degrees of freedom. The method comprises three main steps: (i) the construction of an effective Hamiltonian which describes the dynamics of the relevant degrees of freedom; (ii) the determination of the effective Hamiltonian parameters via

zero-temperature first-principles computations; and (iii) Monte Carlo simulations to determine the finite-temperature behaviour.

3.2.1 Construction of the effective Hamiltonian

The partition function of a system is the primary quantity when studying finite-temperature equilibrium properties. The fact that the terms in the partition sum decreases exponentially with increasing energy motivates our working assumption that the low-temperature partition function can be well approximated by using a simplified energy function which only includes low-energy states. Experiments on $CdCr_2O_4$ and $ZnCr_2O_4$ indicate that the atomic distortions and strain deformations manifested in their respective transition from the cubic phase to the low-symmetry phase are small [49]. We therefore assume that the energetically relevant atomic configurations are close to the cubic structure and that the energy surface around it can be parametrized in terms of a Taylor expansion in the displacements from the cubic structure.

The first step, then, in constructing the effective Hamiltonian consists of identifying the relevant degrees of freedom, which, in addition to atomic distortions and strains, obviously must include spin since the lattice instabilities are driven by magnetic interactions. The spins are treated as classical vectors, an approximation motivated by the rather large magnetic moment of the Cr atoms. The atomic distortions are included in the Taylor series as local modes, i.e. localized real-space atomic displacement patterns. Our choice of local modes consists of the individual displacements of the magnetic ions and distortions of the zinc-centred oxygen tetrahedra. We assume that the effect of the zinc atoms is small and do not include their motion, whereas, on the other hand, a lot of the action presumably involves the magnetic ions so their movement is not restricted. As to the oxygen tetrahedra, the experimental results of the ground state space groups help

us identify which distortions are necessary to include. First note that the transformation properties of the 42 zone-center modes of the $Fd3m$ spinel structure split into the following irreducible representations of O_h [43]:

$$\begin{aligned} \Gamma_{\text{Acoustic}} : &\quad T_{1u} \\ \Gamma_{\text{IR}} : &\quad 4T_{1u} \\ \Gamma_{\text{Raman}} : &\quad A_{1g} \oplus E_g \oplus 3T_{2g} \\ \Gamma_{\text{Silent}} : &\quad 2A_{2u} \oplus 2E_u \oplus T_{1g} \oplus 2T_{2u} \end{aligned} \tag{3.1}$$

Considering $ZnCr_2O_4$, the effective Hamiltonian must be able to generate its proposed ground state structure belonging to $I\overline{4}m2$ [49, 50] or $F222$ [53]. A group-theoretical analysis reveals that the modes transforming according to the two rows of the irreducible representation E_u separately lowers the symmetry from $Fd3m$ to either $I\overline{4}m2$ or $F222$ [43]. Similarly, one finds that the $CdCr_2O_4$ ground state space group $I4_1/amd$ [49] is reached via a distortion of the two oxygen tetrahedra which transform as one of the two rows of E_g. It is possible to describe all of these distortions using a set of four local modes, see Fig. 3.1, which also increases the number of symmetry groups that can be generated by oxygen tetrahedral distortions alone since the two tetrahedra are decoupled. The zone-center modes generated by these four oxygen local modes are E_u ($v_1 + v_2$ and $w_1 + w_2$) and E_g ($v_2 - v_1$ and $w_2 - w_1$). The chromium degrees of freedom generate A_{2u}, E_u, T_{1u}, and T_{2u}. This choice of local modes reduces the size of the atomic configuration space from 14×3 to 16.

The next step in the construction of the effective Hamiltonian consists of deriving its analytical form. Up to second-order terms are included in the expansion and up to third nearest-neighbour Heisenberg exchange interactions. These approximations are based on previous first-principles results for the spin-lattice

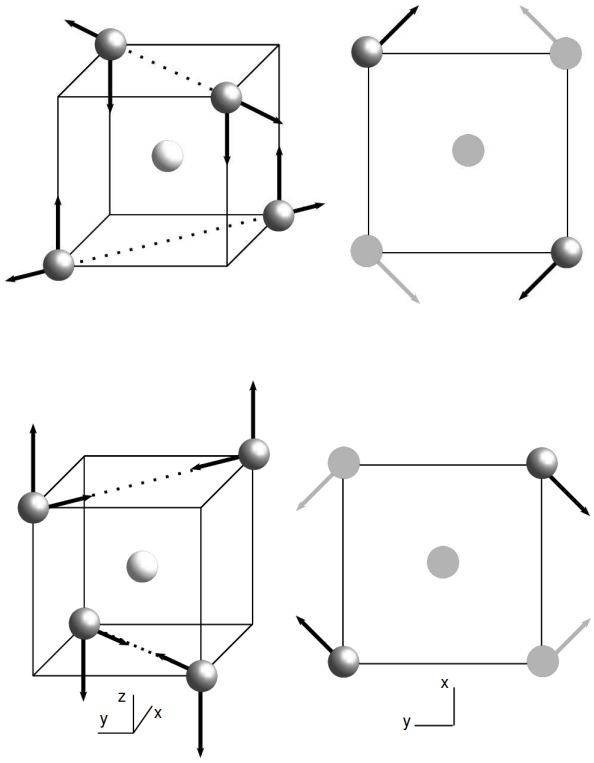

FIGURE 3.1: The four oxygen local modes: v_1 (lower left) and w_1 (lower right) are distortions of the oxygen tetrahedra centred on the $\overline{4}3m$ A-site cation. Similarly, v_2 (upper left) and w_2 (upper right) describe distortions of the oxygen tetrahedra centred the other A-site cation. For v_1 and v_2, the displacement along z is twice that along x and y.

coupling and local moment interactions [54, 55, 57] and the experimental results that the distortions involved in the low-temperature transition are small. If needed, they can be systematically improved by adding higher-order terms and further-neighbour interactions. Mainly for organizational purposes, it is common to let the expansion be invariant with respect to the symmetry group of the reference structure, in our case $Fd3m$. An analysis of the transformation properties of the degrees of freedom under $Fd3m$ yields the precise form of the expansion which is presented in Appendix A (except $H(u_{i\alpha}, v_i, w_i, \eta_i; s_{i\alpha})$ and H_{dipole} which we have not yet derived). Schematically,

$$\begin{aligned} H_{tot} =& H(u_{i\alpha}, v_i, w_i) + H(\eta_i) + H(s_{i\alpha}) + H(u_{i\alpha}, v_i, w_i; \eta_i) \\ &+ H(u_{i\alpha}, v_i, w_i, \eta_i; s_{i\alpha}) + H_{dipole}(u_{i\alpha}, v_i, w_i), \end{aligned}$$

where the local modes are denoted as in Fig. 3.1, $s_{i\alpha}$ ($\alpha = x, y, z$) represents the spin component α on Cr atom i, and η_i ($i = 1 - 6$) is the strain tensor in Voigt notation.

The symmetry analysis leaves us with a set of undetermined parameters. There are to many of them for all to be determined phenomenologically, but they can be determined from independent first-principles calculations.

3.2.2 First-principles calculations

In order to determine the effective Hamiltonian parameters, we have performed density-functional theory calculations within LSDA+U using the VASP code[1] [37, 38] with its supplied PAW potentials [35, 36]. A plane-wave kinetic energy cutoff of 500 eV was used and the Brillouin zone was sampled by a $6 \times 6 \times 6$ Γ-centred k-point grid (for both 14- and 28-atoms cells). For the Berry-phase calculations [39],

[1] Version 4.6.28 of VASP was used.

the mesh was $6 \times 6 \times 12$, with the dense grid in the direction of electronic polarization. Structural relaxations were performed until the forces on the atoms were less than 2.5 meV/Å. Collinear spin configurations were used throughout and no spin-orbit coupling was included. Previous first-principles calculations [54] have found spin-orbit effects to be small; presumably due to Cr^{3+} lacking orbital momentum. The values for the Coulomb on-site repulsion U and exchange parameter j were 3 eV and 0.9 eV, respectively. These values have been used in previous first-principle calculations [54–56], but were not determined from first-principles. Rather, they were chosen as to reproduce certain experimental band gap and photoemission spectral features in other chromium-based spinels.

Force-constant matrices were constructed from finite differences of the forces on symmetry-adapted modes having an amplitude of 0.01 Å. We utilized modes transforming according to the irreducible representations listed in Eq. (3.1) in all computations as this is a complete set (although only for $Fd3m$ structures does it yield block-diagonal force-constant matrices). The derivation of the modes was facilitated by the use of [43])

The three exchange constants J_1, J_2, and J_3—capturing the interaction between first, second, and third nearest neighbours respectively—can be extracted from total-energy computations on cubic structures with four different collinear spin configurations by relating the computed energy with the effective Hamiltonian model. Similar calculations allow us to quantify how the Heisenberg exchange interactions are modified in the presence of local modes and strain.

Coefficients involving local modes can be determined by forming linear combinations of the elements of the force constant matrices of appropriate structures. To be more precise, the procedure consists of writing the first-principles force constant matrix in the basis defined by the local modes and comparing it to the

same matrix as constructed from the analytical expansion. By way of illustration, consider the submatrix that consists of the interaction parameters between v_1, v_2, v_3, and v_4. The expansion yields for the ferromagnetic $Fd3m$ zone-center force-constant matrix:

$$\begin{pmatrix} 2B_1 & 4B_{12} & 0 & 0 \\ & 2B_1 & 0 & 0 \\ & & 2B_1 & 4B_{12} \\ & & & 2B_1 \end{pmatrix} \tag{3.2}$$

where the order of the base vectors is (v_1, v_2, w_1, w_2). Computing the zone-center force-constant matrix of the relaxed $Fd3m$ structure with ferromagnetic spin ordering thus allow us to extract B_1 and B_{12}. In fact, from considering the entire matrix the chromium local modes parameters $A_x, A_{xy}, \overline{A}_{xx}, \overline{A}_{zz}, \overline{A}_{xy}, \overline{A}_{xz}$ can also be determined. This zone-center computation does not, however, provide enough information to determine the coupling coefficients between chromium and oxygen local modes. One way to produce the necessary supplementary equations are through cumbersome—due to the large cell required—zone-boundary computations. An alternative approach, which eliminates the need for additional computations but also introduces further approximations, is to keep only two coupling coefficients. The complication then is how to perform this reduction without resorting to guesswork.

By recomputing the force constant matrix for strained structures and different spin arrangements we can determine the coupling between the local modes, strain, and spin; consider, e.g., the change in (3.2) due to a strain along the z-axis

($\eta_3 \neq 0$):

$$2\eta_3 \times \begin{pmatrix} k_1 & l_1 & 0 & 0 \\ & k_1 & 0 & 0 \\ & & k_2 & l_2 \\ & & & k_2 \end{pmatrix}$$

where

$$\begin{aligned} k_1 &= \frac{1}{2}L_{xxv} + L_{zzv} + \frac{3}{2}L_{xxw} + 2L_{xxvw}, \\ k_2 &= \frac{3}{2}L_{xxv} + L_{zzw} + \frac{1}{2}L_{xxw} - 2L_{xxvw}, \\ l_1 &= \overline{L}_{xxv} + L_{zzv} + 3\overline{L}_{xxw} + 2\overline{L}_{xxvw}, \\ \text{and} \quad l_2 &= 3\overline{L}_{xxv} + L_{zzw} + \overline{L}_{xxw} - 2\overline{L}_{xxvw}. \end{aligned}$$

Analogous computations with other combinations of non-zero η_1, η_2, and η_3 provide the additional equations necessary to determine the coupling coefficients between the four oxygen local modes and strain (but all the coupling coefficients between the chromium local modes and the diagonal strain tensor components can actually be determined from this computations).

3.3 Results

Optimizations in the $Fd3m$ space group of the lattice parameter a and anion parameter u (for the origin is $4\overline{4}3m$ on an A-site cation) resulted in $a = 8.534$ Å and $u = 0.394$ for $CdCr_2O_4$ and $a = 8.255$ Å and $u = 0.386$ for $ZnCr_2O_4$. The Born effective charges are listed in Table 3.1 and the zone-center phonon frequencies in Table 3.2. The effective Hamiltonian terms that have been derived are listed in Appendix A and the parameters determined thus far are reported in Table 3.3.

TABLE 3.1: Born effective charges for the two AB_2X_4 spinels. The subscripts 1 and 2 refer to the diagonal and off-diagonal entries, respectively, of the Born effective charge tensor.

	$CdCr_2O_4$	$ZnCr_2O_4$
Z^*(A)	2.32	2.26
Z_1^*(B)	3.00	2.95
Z_2^*(B)	−0.73	−0.59
Z_1^*(X)	−2.07	−2.04
Z_2^*(X)	0.07	0.02

TABLE 3.2: Phonon frequencies in cm^{-1} of the ferromagnetic $Fd3m$ structures.

	$CdCr_2O_4$	$ZnCr_2O_4$
A_{1g}	695	688
A_{2u}	480	503
	676	667
E_g	463	471
E_u	324	338
	478	505
T_{1g}	424	449
T_{1u}	157	195
	379	389
	488	510
	616	614
T_{2g}	132	180
	505	518
	603	609
T_{2u}	198	204
	449	478

TABLE 3.3: First-principles effective Hamiltonian parameters in eV/Å^2 per primitive unit cell.

	$CdCr_2O_4$	$ZnCr_2O_4$
A_x	11.90	13.08
A_{xy}	2.28	3.13
$\overline{A}_{xx}$	−1.17	−1.42
$\overline{A}_{zz}$	0.27	0.35
$\overline{A}_{xy}$	−2.74	−3.10
$\overline{A}_{xz}$	0.08	0.01
B_1	6.46	6.91
B_{12}	0.07	0.19

3.4 Outlook

The dipole-dipole part of the Hamiltonian and the part describing how the Heisenberg exchange interaction is modulated by the local modes and strain have not been derived yet. Furthermore, as mentioned in Sec. 3.2.2, computations on cells larger than the primitive unit cell are necessary to determine the coupling coefficients between the chromium and oxygen local modes. The same difficulty arises with the coupling between the oxygen local modes and shear. Alternatively, one includes fewer terms in the expansion; we have investigated this method which requires a systematic procedure to reduce the number of coefficients.

When the determination and validation of the coefficients are finished, finite-temperature behaviour can be studied using Monte Carlo simulations. We have written a computer programme that solves the effective Hamiltonian by means of the Metropolis algorithm [58]. The code is ready except for the implementation of the energy terms mentioned above. This technique enables the modelling of systems with sizes completely impractical to treat directly from first-principles,

allowing, e.g., for complex spin orderings requiring large supercells. With this machinery at one's disposal, one can hopefully clarify the role of spin-lattice coupling in the transitions to the antiferromagnetic ground states. By comparing the results for $CdCr_2O_4$ and $ZnCr_2O_4$, one may also gain additional insight into the different ways to relieve frustration that are compatible with the spinel structure.

Appendix A
The Spinel Effective Hamiltonian

The terms of the spinel effective Hamiltonian derived thus far are listed in this Appendix. All terms are summed over $\mathbf{R} = n_1\mathbf{t_1} + n_2\mathbf{t_2} + n_3\mathbf{t_3}$, where $\mathbf{t_1} = a(0,1,1)/2$, $\mathbf{t_2} = a(1,0,1)/2$, and $\mathbf{t_3} = a(1,1,0)/2$ are the lattice vectors of the cubic spinel primitive unit cell. The origin is at $\overline{4}3m$ on an A-site cation. Many obvious plus signs are suppressed in the formulae and the following shorthand notation is used: $u_{i\alpha} \equiv u_{i\alpha}(\mathbf{R})$, $v_i \equiv v_i(\mathbf{R})$, $w_i \equiv w_i(\mathbf{R})$, $\mathbf{S}_i \equiv \mathbf{S}_i(\mathbf{R})$, $u_{i\alpha}v_j(\mathbf{R}+\mathbf{\Delta}) \equiv u_{i\alpha}(\mathbf{R})v_j(\mathbf{R}+\mathbf{\Delta})$, $\alpha = 1/2$ and $\beta = \sqrt{3}/2$.

$$\frac{J_1}{2}\sum_{\text{n.n.}} \mathbf{S}_i \cdot \mathbf{S}_j + \frac{J_2}{2}\sum_{2^{\text{nd}}\text{ n.n.}} \mathbf{S}_i \cdot \mathbf{S}_j + \frac{J_3}{2}\sum_{3^{\text{rd}}\text{ n.n.}} \mathbf{S}_i \cdot \mathbf{S}_j$$

$$A_x \sum_{n=1}^{4} \sum_{\alpha=x,y,z} [u_{n\alpha}(\mathbf{R})]^2$$

$$A_{xy}\Big(\begin{array}{ccc} u_{1x}u_{1y} & u_{1x}u_{1z} & u_{1y}u_{1z} \\ u_{2x}u_{2y} & -u_{2x}u_{2z} & -u_{2y}u_{2z} \\ -u_{3x}u_{3y} & u_{3x}u_{3z} & -u_{3y}u_{3z} \\ -u_{4x}u_{4y} & -u_{4x}u_{4z} & u_{4y}u_{4z} \end{array} \Big)$$

$$\overline{A}_{zz}\Big(\begin{array}{cccc} u_{1z}u_{2z} & u_{1z}(\mathbf{R})u_{2z}(\mathbf{R}-\mathbf{t_3}) & u_{2x}u_{3x} & u_{2x}(\mathbf{R})u_{3x}(\mathbf{R}-\mathbf{t_2}+\mathbf{t_3}) \\ u_{1y}u_{3y} & u_{1y}(\mathbf{R})u_{3y}(\mathbf{R}-\mathbf{t_2}) & u_{2y}u_{4y} & u_{2y}(\mathbf{R})u_{4y}(\mathbf{R}-\mathbf{t_1}+\mathbf{t_3}) \\ u_{1x}u_{4x} & u_{1x}(\mathbf{R})u_{4x}(\mathbf{R}-\mathbf{t_1}) & u_{3z}u_{4z} & u_{3z}(\mathbf{R})u_{4z}(\mathbf{R}-\mathbf{t_1}+\mathbf{t_2}) \end{array} \Big)$$

$$
\overline{A}_{xx}\Big(\begin{array}{cccc}
u_{1x}u_{2x} & u_{1x}(\mathbf{R})u_{2x}(\mathbf{R}-\mathbf{t_3}) & u_{1y}u_{2y} & u_{1y}(\mathbf{R})u_{2y}(\mathbf{R}-\mathbf{t_3}) \\
u_{1z}u_{3z} & u_{1z}(\mathbf{R})u_{3z}(\mathbf{R}-\mathbf{t_2}) & u_{1x}u_{3x} & u_{1x}(\mathbf{R})u_{3x}(\mathbf{R}-\mathbf{t_2}) \\
u_{1y}u_{4y} & u_{1y}(\mathbf{R})u_{4y}(\mathbf{R}-\mathbf{t_1}) & u_{1z}u_{4z} & u_{1z}(\mathbf{R})u_{4z}(\mathbf{R}-\mathbf{t_1}) \\
u_{2y}u_{3y} & u_{2y}(\mathbf{R})u_{3y}(\mathbf{R}-\mathbf{t_2}+\mathbf{t_3}) & u_{2z}u_{3z} & u_{2z}(\mathbf{R})u_{3z}(\mathbf{R}-\mathbf{t_2}+\mathbf{t_3}) \\
u_{2z}u_{4z} & u_{2z}(\mathbf{R})u_{4z}(\mathbf{R}-\mathbf{t_1}+\mathbf{t_3}) & u_{2x}u_{4x} & u_{2x}(\mathbf{R})u_{4x}(\mathbf{R}-\mathbf{t_1}+\mathbf{t_3}) \\
u_{3x}u_{4x} & u_{3x}(\mathbf{R})u_{4x}(\mathbf{R}-\mathbf{t_1}+\mathbf{t_2}) & u_{3y}u_{4y} & u_{3y}(\mathbf{R})u_{4y}(\mathbf{R}-\mathbf{t_1}+\mathbf{t_2})
\end{array} \Big)
$$

$$
\overline{A}_{xy}\Big(\begin{array}{cccc}
u_{1x}u_{2y} & u_{1y}(\mathbf{R})u_{2x}(\mathbf{R}-\mathbf{t_3}) & -u_{2y}u_{3z} & -u_{2z}(\mathbf{R})u_{3y}(\mathbf{R}-\mathbf{t_2}+\mathbf{t_3}) \\
u_{2x}u_{1y} & u_{2y}(\mathbf{R})u_{1x}(\mathbf{R}+\mathbf{t_3}) & -u_{3y}u_{2z} & -u_{3z}(\mathbf{R})u_{2y}(\mathbf{R}+\mathbf{t_2}-\mathbf{t_3}) \\
u_{1z}u_{3x} & u_{1x}(\mathbf{R})u_{3z}(\mathbf{R}-\mathbf{t_2}) & -u_{2z}u_{4x} & -u_{2x}(\mathbf{R})u_{4z}(\mathbf{R}-\mathbf{t_1}+\mathbf{t_3}) \\
u_{3z}u_{1x} & u_{3x}(\mathbf{R})u_{1z}(\mathbf{R}+\mathbf{t_2}) & -u_{4z}u_{2x} & -u_{4x}(\mathbf{R})u_{2z}(\mathbf{R}+\mathbf{t_1}-\mathbf{t_3}) \\
u_{1y}u_{4z} & u_{1z}(\mathbf{R})u_{4y}(\mathbf{R}-\mathbf{t_1}) & -u_{3x}u_{4y} & -u_{3y}(\mathbf{R})u_{4x}(\mathbf{R}-\mathbf{t_1}+\mathbf{t_2}) \\
u_{4y}u_{1z} & u_{4z}(\mathbf{R})u_{1y}(\mathbf{R}+\mathbf{t_1}) & -u_{4x}u_{3y} & -u_{4y}(\mathbf{R})u_{3x}(\mathbf{R}+\mathbf{t_1}-\mathbf{t_2})
\end{array} \Big)
$$

$$
\overline{A}_{xz}\Big(\begin{array}{cccc}
u_{1x}u_{2z} & u_{1x}(\mathbf{R})u_{2z}(\mathbf{R}-\mathbf{t_3}) & u_{1y}u_{2z} & u_{1y}(\mathbf{R})u_{2z}(\mathbf{R}-\mathbf{t_3}) \\
-u_{2x}u_{1z} & -u_{2x}(\mathbf{R})u_{1z}(\mathbf{R}+\mathbf{t_3}) & -u_{2y}u_{1z} & -u_{2y}(\mathbf{R})u_{1z}(\mathbf{R}+\mathbf{t_3}) \\
u_{1z}u_{3y} & u_{1z}(\mathbf{R})u_{3y}(\mathbf{R}-\mathbf{t_2}) & u_{1x}u_{3y} & u_{1x}(\mathbf{R})u_{3y}(\mathbf{R}-\mathbf{t_2}) \\
-u_{3z}u_{1y} & -u_{3z}(\mathbf{R})u_{1y}(\mathbf{R}+\mathbf{t_2}) & -u_{3x}u_{1y} & -u_{3x}(\mathbf{R})u_{1y}(\mathbf{R}+\mathbf{t_2}) \\
u_{1y}u_{4x} & u_{1y}(\mathbf{R})u_{4x}(\mathbf{R}-\mathbf{t_1}) & u_{1z}u_{4x} & u_{1z}(\mathbf{R})u_{4x}(\mathbf{R}-\mathbf{t_1}) \\
-u_{4y}u_{1x} & -u_{4y}(\mathbf{R})u_{1x}(\mathbf{R}+\mathbf{t_1}) & -u_{4z}u_{1x} & -u_{4z}(\mathbf{R})u_{1x}(\mathbf{R}+\mathbf{t_1}) \\
u_{2y}u_{3x} & u_{2y}(\mathbf{R})u_{3x}(\mathbf{R}-\mathbf{t_2}+\mathbf{t_3}) & -u_{2z}u_{3x} & -u_{2z}(\mathbf{R})u_{3x}(\mathbf{R}-\mathbf{t_2}+\mathbf{t_3}) \\
-u_{3y}u_{2x} & -u_{3y}(\mathbf{R})u_{2x}(\mathbf{R}+\mathbf{t_2}-\mathbf{t_3}) & u_{3z}u_{2x} & u_{3z}(\mathbf{R})u_{2x}(\mathbf{R}+\mathbf{t_2}-\mathbf{t_3}) \\
-u_{2z}u_{4y} & -u_{2z}(\mathbf{R})u_{4y}(\mathbf{R}-\mathbf{t_1}+\mathbf{t_3}) & u_{2x}u_{4y} & u_{2x}(\mathbf{R})u_{4y}(\mathbf{R}-\mathbf{t_1}+\mathbf{t_3}) \\
u_{4z}u_{2y} & u_{4z}(\mathbf{R})u_{2y}(\mathbf{R}+\mathbf{t_1}-\mathbf{t_3}) & -u_{4x}u_{2y} & -u_{4x}(\mathbf{R})u_{2y}(\mathbf{R}+\mathbf{t_1}-\mathbf{t_3}) \\
u_{3x}u_{4z} & u_{3x}(\mathbf{R})u_{4z}(\mathbf{R}-\mathbf{t_1}+\mathbf{t_2}) & -u_{3y}u_{4z} & -u_{3y}(\mathbf{R})u_{4z}(\mathbf{R}-\mathbf{t_1}+\mathbf{t_2}) \\
-u_{4x}u_{3z} & -u_{4x}(\mathbf{R})u_{3z}(\mathbf{R}+\mathbf{t_1}-\mathbf{t_2}) & u_{4y}u_{3z} & u_{4y}(\mathbf{R})u_{3z}(\mathbf{R}+\mathbf{t_1}-\mathbf{t_2})
\end{array} \Big)
$$

$$B_{12}\Big(v_1v_2 + v_1(\mathbf{R})v_2(\mathbf{R}-\mathbf{t_1}) + v_1(\mathbf{R})v_2(\mathbf{R}-\mathbf{t_2}) + v_1(\mathbf{R})v_2(\mathbf{R}-\mathbf{t_3})$$
$$w_1w_2 + w_1(\mathbf{R})w_2(\mathbf{R}-\mathbf{t_1}) + w_1(\mathbf{R})w_2(\mathbf{R}-\mathbf{t_2}) + w_1(\mathbf{R})w_2(\mathbf{R}-\mathbf{t_3})\Big)$$

$$B_1\Big(v_1^2 + v_2^2 + w_1^2 + w_2^2\Big)$$

$$C_{11}\Big(\eta_1^2 + \eta_2^2 + \eta_3^2\Big)$$

$$C_{12}\Big(\eta_1\eta_2 + \eta_1\eta_3 + \eta_2\eta_3\Big)$$

$$C_{44}\Big(\eta_6^2 + \eta_5^2 + \eta_4^2\Big)$$

$$K_{xxxx}\sum_{i=1}^{4}\Big(\eta_1u_{ix}^2 + \eta_2u_{iy}^2 + \eta_3u_{iz}^2\Big)$$

$$K_{xxyy}\sum_{i=1}^{4}\Big(\eta_1\big(u_{iy}^2 + u_{iz}^2\big) + \eta_2\big(u_{ix}^2 + u_{iz}^2\big) + \eta_3\big(u_{ix}^2 + u_{iy}^2\big)\Big)$$

$$\begin{aligned} K_{xxxy}\Big(\quad & \big(\eta_1+\eta_2\big)\big(u_{1x}u_{1y} + u_{2x}u_{2y} - u_{3x}u_{3y} - u_{4x}u_{4y}\big) \\ + \quad & \big(\eta_1+\eta_3\big)\big(u_{1x}u_{1z} - u_{2x}u_{2z} + u_{3x}u_{3z} - u_{4x}u_{4z}\big) \\ + \quad & \big(\eta_2+\eta_3\big)\big(u_{1y}u_{1z} - u_{2y}u_{2z} - u_{3y}u_{3z} + u_{4y}u_{4z}\big) \quad \Big) \end{aligned}$$

$$\begin{aligned} K_{xxyz}\Big(\quad & \eta_1\big(u_{1y}u_{1z} - u_{2y}u_{2z} - u_{3y}u_{3z} + u_{4y}u_{4z}\big) \\ + \quad & \eta_2\big(u_{1x}u_{1z} - u_{2x}u_{2z} + u_{3x}u_{3z} - u_{4x}u_{4z}\big) \\ + \quad & \eta_3\big(u_{1x}u_{1y} + u_{2x}u_{2y} - u_{3x}u_{3y} - u_{4x}u_{4y}\big) \quad \Big) \end{aligned}$$

$$\begin{aligned} K_{xyxx}\Big(\quad & \eta_6\big(u_{1x}^2 + u_{2x}^2 - u_{3x}^2 - u_{4x}^2 + (x\to y)\big) \\ + \quad & \eta_5\big(u_{1x}^2 - u_{2x}^2 + u_{3x}^2 - u_{4x}^2 + (x\to z)\big) \\ + \quad & \eta_4\big(u_{1y}^2 - u_{2y}^2 - u_{3y}^2 + u_{4y}^2 + (y\to z)\big) \quad \Big) \end{aligned}$$

$$\begin{aligned} K_{xyzz}\Big(\quad & \eta_6\big(u_{1z}^2 + u_{2z}^2 - u_{3z}^2 - u_{4z}^2\big) \\ + \quad & \eta_5\big(u_{1y}^2 - u_{2y}^2 + u_{3y}^2 - u_{4y}^2\big) \\ + \quad & \eta_4\big(u_{1x}^2 - u_{2x}^2 - u_{3x}^2 + u_{4x}^2\big) \quad \Big) \end{aligned}$$

$$
\begin{aligned}
K_{xyxz}\Big(\quad & \eta_6\big(u_{1x}u_{1z} - u_{2x}u_{2z} - u_{3x}u_{3z} + u_{4x}u_{4z} \\
& + u_{1y}u_{1z} - u_{2y}u_{2z} + u_{3y}u_{3z} - u_{4y}u_{4z}\big) \\
& + \eta_5\big(u_{1x}u_{1y} - u_{2x}u_{2y} - u_{3x}u_{3y} + u_{4x}u_{4y} \\
& + u_{1y}u_{1z} + u_{2y}u_{2z} - u_{3y}u_{3z} - u_{4y}u_{4z}\big) \\
& + \eta_4\big(u_{1x}u_{1y} - u_{2x}u_{2y} + u_{3x}u_{3y} - u_{4x}u_{4y} \\
& + u_{1x}u_{1z} + u_{2x}u_{2z} - u_{3x}u_{3z} - u_{4x}u_{4z}\big) \quad \Big)
\end{aligned}
$$

$$
K_{xyxy}\sum_{i=1}^{4}\Big(\eta_6 u_{ix}u_{iy} + \eta_5 u_{ix}u_{iz} + \eta_4 u_{iy}u_{iz}\Big)
$$

$$
\begin{aligned}
L\Big(\quad & \eta_1\big((1-\alpha)v_1 + \beta w_1 - (1-\alpha)v_2 - \beta w_2\big) \\
+ \quad & \eta_2\big((1-\alpha)v_1 - \beta w_1 - (1-\alpha)v_2 + \beta w_2\big) \\
+ \quad & \eta_3\big(-2\alpha v_1 + 2\alpha v_2\big)\Big)
\end{aligned}
$$

$$
\begin{aligned}
L_{xxv}\sum_{i=1,2}\Big(\quad & \eta_1\big((1+\alpha^2)v_i^2 - 2\alpha\beta v_i w_i + \beta^2 w_i^2\big) \\
& + \eta_2\big((1+\alpha^2)v_i^2 + 2\alpha\beta v_i w_i + \beta^2 w_i^2\big) + \eta_3 2\big(\alpha^2 v_i^2 + \beta^2 w_i^2\big)\Big)
\end{aligned}
$$

$$
L_{zzv}\sum_{i=1,2}\Big(\eta_1\big(\alpha^2 v_i^2 + 2\alpha\beta v_i w_i + \beta^2 w_i^2\big) + \eta_2\big(\alpha^2 v_i^2 - 2\alpha\beta v_i w_i + \beta^2 w_i^2\big) + \eta_3 v_i^2\Big)
$$

$$
\begin{aligned}
L_{xxw}\sum_{i=1,2}\Big(\quad & \eta_1\big(\beta^2 v_i^2 + 2\alpha\beta v_i w_i + (1+\alpha^2)w_i^2\big) \\
& + \eta_2\big(\beta^2 v_i^2 - 2\alpha\beta v_i w_i + (1+\alpha^2)w_i^2\big) + \eta_3 2\big(\beta^2 v_i^2 + \alpha^2 w_i^2\big)\Big)
\end{aligned}
$$

$$
\begin{aligned}
L_{zzw}\sum_{i=1,2}\Big(\quad & \eta_1\big(\beta^2 v_i^2 - 2\alpha\beta v_i w_i + \alpha^2 w_i^2\big) \\
& + \eta_2\big(\beta^2 v_i^2 + 2\alpha\beta v_i w_i + \alpha^2 w_i^2\big) + \eta_3 w_i^2\Big)
\end{aligned}
$$

$$
\begin{aligned}
L_{xxvw}\sum_{i=1,2}\Big(\eta_1\big(-\alpha\beta v_i^2 + (1-\alpha^2+\beta^2)v_i w_i + \alpha\beta w_i^2\big) \\
- \eta_2\big(\alpha\beta v_i^2 + (1-\alpha^2+\beta^2)v_i w_i - \alpha\beta w_i^2\big) + \eta_3 2\alpha\beta\big(v_i^2 - w_i^2\big)\Big)
\end{aligned}
$$

$$
\begin{aligned}
C_{3xv1}\Big(& -u_{1x}v_1(\mathbf{R}+\mathbf{t_1}+\mathbf{t_2}-\mathbf{t_3}) && \alpha u_{1z}v_1(\mathbf{R}+\mathbf{t_1}) && \alpha u_{1y}v_1(\mathbf{R}+\mathbf{t_2}) \\
& && -\beta u_{1z}w_1(\mathbf{R}+\mathbf{t_1}) && \beta u_{1y}w_1(\mathbf{R}+\mathbf{t_2}) \\
& -u_{1y}v_2(\mathbf{R}) && \alpha u_{1x}v_2(\mathbf{R}+\mathbf{t_2}-\mathbf{t_3}) && \alpha u_{1z}v_2(\mathbf{R}+\mathbf{t_1}-\mathbf{t_3}) \\
& && -\beta u_{1x}w_2(\mathbf{R}+\mathbf{t_2}-\mathbf{t_3}) && \beta u_{1z}w_2(\mathbf{R}+\mathbf{t_1}-\mathbf{t_3}) \\
& u_{2x}v_1(\mathbf{R}+\mathbf{t_1}+\mathbf{t_2}) && -\alpha u_{2y}v_1(\mathbf{R}+\mathbf{t_1}) && \alpha u_{2z}v_1(\mathbf{R}+\mathbf{t_2}) \\
& && -\beta u_{2y}w_1(\mathbf{R}+\mathbf{t_1}) && -\beta u_{2z}w_1(\mathbf{R}+\mathbf{t_2}) \\
& u_{2y}v_2(\mathbf{R}) && -\alpha u_{2x}v_2(\mathbf{R}+\mathbf{t_1}) && \alpha u_{2z}v_2(\mathbf{R}+\mathbf{t_2}) \\
& && \beta u_{2x}w_2(\mathbf{R}+\mathbf{t_1}) && \beta u_{2z}w_2(\mathbf{R}+\mathbf{t_2}) \\
& u_{3x}v_1(\mathbf{R}+\mathbf{t_2}) && -\alpha u_{3z}v_1(\mathbf{R}+\mathbf{t_1}+\mathbf{t_2}) && \alpha u_{3y}v_1(\mathbf{R}+\mathbf{t_1}+\mathbf{t_2}-\mathbf{t_3}) \\
& && \beta u_{3z}w_1(\mathbf{R}+\mathbf{t_1}+\mathbf{t_2}) && \beta u_{3y}w_1(\mathbf{R}+\mathbf{t_1}+\mathbf{t_2}-\mathbf{t_3}) \\
& -u_{3y}v_2(\mathbf{R}+\mathbf{t_1}+\mathbf{t_2}-\mathbf{t_3}) && -\alpha u_{3z}v_2(\mathbf{R}+\mathbf{t_2}) && -\alpha u_{3x}v_2(\mathbf{R}+\mathbf{t_2}-\mathbf{t_3}) \\
& && -\beta u_{3z}w_2(\mathbf{R}+\mathbf{t_2}) && \beta u_{3x}w_2(\mathbf{R}+\mathbf{t_2}-\mathbf{t_3}) \\
& -u_{4x}v_1(\mathbf{R}+\mathbf{t_1}) && -\alpha u_{4y}v_1(\mathbf{R}+\mathbf{t_1}+\mathbf{t_2}) && -\alpha u_{4z}v_1(\mathbf{R}+\mathbf{t_1}+\mathbf{t_2}-\mathbf{t_3}) \\
& && -\beta u_{4y}w_1(\mathbf{R}+\mathbf{t_1}+\mathbf{t_2}) && \beta u_{4z}w_1(\mathbf{R}+\mathbf{t_1}+\mathbf{t_2}-\mathbf{t_3}) \\
& u_{4y}v_2(\mathbf{R}+\mathbf{t_1}+\mathbf{t_2}-\mathbf{t_3}) && \alpha u_{4x}v_2(\mathbf{R}+\mathbf{t_1}) && -\alpha u_{4z}v_2(\mathbf{R}+\mathbf{t_1}-\mathbf{t_3}) \\
& && -\beta u_{4x}w_2(\mathbf{R}+\mathbf{t_1}) && -\beta u_{4z}w_2(\mathbf{R}+\mathbf{t_1}-\mathbf{t_3}) \\
& -\big(u_{1y}v_1(\mathbf{R}+\mathbf{t_1}+\mathbf{t_2}-\mathbf{t_3}) && -\alpha u_{1z}v_1(\mathbf{R}+\mathbf{t_2}) && -\alpha u_{1x}v_1(\mathbf{R}+\mathbf{t_1}) \\
& && -\beta u_{1z}w_1(\mathbf{R}+\mathbf{t_2}) && \beta u_{1x}w_1(\mathbf{R}+\mathbf{t_1}) \\
& u_{1x}v_2(\mathbf{R}) && -\alpha u_{1y}v_2(\mathbf{R}+\mathbf{t_1}-\mathbf{t_3}) && -\alpha u_{1z}v_2(\mathbf{R}+\mathbf{t_2}-\mathbf{t_3}) \\
& && -\beta u_{1y}w_2(\mathbf{R}+\mathbf{t_1}-\mathbf{t_3}) && \beta u_{1z}w_2(\mathbf{R}+\mathbf{t_2}-\mathbf{t_3}) \\
& -u_{2y}v_1(\mathbf{R}+\mathbf{t_1}+\mathbf{t_2}) && \alpha u_{2x}v_1(\mathbf{R}+\mathbf{t_2}) && -\alpha u_{2z}v_1(\mathbf{R}+\mathbf{t_1}) \\
& && -\beta u_{2x}w_1(\mathbf{R}+\mathbf{t_2}) && -\beta u_{2z}w_1(\mathbf{R}+\mathbf{t_1}) \\
& -u_{2x}v_2(\mathbf{R}) && \alpha u_{2y}v_2(\mathbf{R}+\mathbf{t_2}) && -\alpha u_{2z}v_2(\mathbf{R}+\mathbf{t_1}) \\
& && \beta u_{2y}w_2(\mathbf{R}+\mathbf{t_2}) && \beta u_{2z}w_2(\mathbf{R}+\mathbf{t_1}) \\
& u_{3y}v_1(\mathbf{R}+\mathbf{t_2}) && \alpha u_{3x}v_1(\mathbf{R}+\mathbf{t_1}+\mathbf{t_2}) && \alpha u_{3z}v_1(\mathbf{R}+\mathbf{t_1}+\mathbf{t_2}-\mathbf{t_3}) \\
& && -\beta u_{3x}w_1(\mathbf{R}+\mathbf{t_1}+\mathbf{t_2}) && \beta u_{3z}w_1(\mathbf{R}+\mathbf{t_1}+\mathbf{t_2}-\mathbf{t_3}) \\
& -u_{3x}v_2(\mathbf{R}+\mathbf{t_1}+\mathbf{t_2}-\mathbf{t_3}) && -\alpha u_{3y}v_2(\mathbf{R}+\mathbf{t_2}) && \alpha u_{3z}v_2(\mathbf{R}+\mathbf{t_2}-\mathbf{t_3}) \\
& && -\beta u_{3y}w_2(\mathbf{R}+\mathbf{t_2}) && -\beta u_{3z}w_2(\mathbf{R}+\mathbf{t_2}-\mathbf{t_3}) \\
& -u_{4y}v_1(\mathbf{R}+\mathbf{t_1}) && \alpha u_{4z}v_1(\mathbf{R}+\mathbf{t_1}+\mathbf{t_2}) && -\alpha u_{4x}v_1(\mathbf{R}+\mathbf{t_1}+\mathbf{t_2}-\mathbf{t_3}) \\
& && \beta u_{4z}w_1(\mathbf{R}+\mathbf{t_1}+\mathbf{t_2}) && \beta u_{4x}w_1(\mathbf{R}+\mathbf{t_1}+\mathbf{t_2}-\mathbf{t_3}) \\
& u_{4x}v_2(\mathbf{R}+\mathbf{t_1}+\mathbf{t_2}-\mathbf{t_3}) && \alpha u_{4z}v_2(\mathbf{R}+\mathbf{t_1}) && \alpha u_{4y}v_2(\mathbf{R}+\mathbf{t_1}-\mathbf{t_3}) \\
& && -\beta u_{4z}w_2(\mathbf{R}+\mathbf{t_1}) && \beta u_{4y}w_2(\mathbf{R}+\mathbf{t_1}-\mathbf{t_3})\big)\Big)
\end{aligned}
$$

$$
\begin{aligned}
C_{3xw1}\Big(& -u_{1x}w_1(\mathbf{R}+\mathbf{t_1}+\mathbf{t_2}-\mathbf{t_3}) && \alpha u_{1z}w_1(\mathbf{R}+\mathbf{t_1}) && \alpha u_{1y}w_1(\mathbf{R}+\mathbf{t_1}+\mathbf{t_2}) \\
& && \beta u_{1z}v_1(\mathbf{R}+\mathbf{t_1}) && -\beta u_{1y}v_1(\mathbf{R}+\mathbf{t_1}+\mathbf{t_2}) \\
& u_{1y}w_2(\mathbf{R}) && -\alpha u_{1x}w_2(\mathbf{R}+\mathbf{t_2}-\mathbf{t_3}) && -\alpha u_{1z}w_2(\mathbf{R}+\mathbf{t_1}-\mathbf{t_3}) \\
& && -\beta u_{1x}v_2(\mathbf{R}+\mathbf{t_2}-\mathbf{t_3}) && \beta u_{1z}v_2(\mathbf{R}+\mathbf{t_1}-\mathbf{t_3}) \\
& u_{2x}w_1(\mathbf{R}+\mathbf{t_1}+\mathbf{t_2}) && -\alpha u_{2y}w_1(\mathbf{R}+\mathbf{t_1}) && \alpha u_{2z}w_1(\mathbf{R}+\mathbf{t_2}) \\
& && \beta u_{2y}v_1(\mathbf{R}+\mathbf{t_1}) && \beta u_{2z}v_1(\mathbf{R}+\mathbf{t_2}) \\
& -u_{2y}w_2(\mathbf{R}) && \alpha u_{2x}w_2(\mathbf{R}+\mathbf{t_1}) && -\alpha u_{2z}w_2(\mathbf{R}+\mathbf{t_2}) \\
& && \beta u_{2x}v_2(\mathbf{R}+\mathbf{t_1}) && \beta u_{2z}v_2(\mathbf{R}+\mathbf{t_2}) \\
& u_{3x}w_1(\mathbf{R}+\mathbf{t_2}) && -\alpha u_{3z}w_1(\mathbf{R}+\mathbf{t_1}+\mathbf{t_2}) && \alpha u_{3y}w_1(\mathbf{R}+\mathbf{t_1}+\mathbf{t_2}-\mathbf{t_3}) \\
& && -\beta u_{3z}v_1(\mathbf{R}+\mathbf{t_1}+\mathbf{t_2}) && -\beta u_{3y}v_1(\mathbf{R}+\mathbf{t_1}+\mathbf{t_2}-\mathbf{t_3}) \\
& u_{3y}w_2(\mathbf{R}+\mathbf{t_1}+\mathbf{t_2}-\mathbf{t_3}) && \alpha u_{3z}w_2(\mathbf{R}+\mathbf{t_2}) && \alpha u_{3x}w_2(\mathbf{R}+\mathbf{t_2}-\mathbf{t_3}) \\
& && -\beta u_{3z}v_2(\mathbf{R}+\mathbf{t_2}) && \beta u_{3x}v_2(\mathbf{R}+\mathbf{t_2}-\mathbf{t_3}) \\
& -u_{4x}w_1(\mathbf{R}+\mathbf{t_1}) && -\alpha u_{4y}w_1(\mathbf{R}+\mathbf{t_1}+\mathbf{t_2}) && -\alpha u_{4z}w_1(\mathbf{R}+\mathbf{t_1}+\mathbf{t_2}-\mathbf{t_3}) \\
& && \beta u_{4y}v_1(\mathbf{R}+\mathbf{t_1}+\mathbf{t_2}) && -\beta u_{4z}v_1(\mathbf{R}+\mathbf{t_1}+\mathbf{t_2}-\mathbf{t_3}) \\
& -u_{4y}w_2(\mathbf{R}+\mathbf{t_1}+\mathbf{t_2}-\mathbf{t_3}) && -\alpha u_{4x}w_2(\mathbf{R}+\mathbf{t_1}) && \alpha u_{4z}w_2(\mathbf{R}+\mathbf{t_1}-\mathbf{t_3}) \\
& && -\beta u_{4x}v_2(\mathbf{R}+\mathbf{t_1}) && -\beta u_{4z}v_2(\mathbf{R}+\mathbf{t_1}-\mathbf{t_3}) \\
-\big(& -u_{1y}w_1(\mathbf{R}+\mathbf{t_1}+\mathbf{t_2}-\mathbf{t_3}) && \alpha u_{1z}w_1(\mathbf{R}+\mathbf{t_2}) && \alpha u_{1x}w_1(\mathbf{R}+\mathbf{t_1}) \\
& && -\beta u_{1z}v_1(\mathbf{R}+\mathbf{t_2}) && \beta u_{1x}v_1(\mathbf{R}+\mathbf{t_1}) \\
& u_{1x}w_2(\mathbf{R}) && -\alpha u_{1y}w_2(\mathbf{R}+\mathbf{t_1}-\mathbf{t_3}) && -\alpha u_{1z}w_2(\mathbf{R}+\mathbf{t_2}-\mathbf{t_3}) \\
& && \beta u_{1y}v_2(\mathbf{R}+\mathbf{t_1}-\mathbf{t_3}) && -\beta u_{1z}v_2(\mathbf{R}+\mathbf{t_2}-\mathbf{t_3}) \\
& u_{2y}w_1(\mathbf{R}+\mathbf{t_1}+\mathbf{t_2}) && -\alpha u_{2x}w_1(\mathbf{R}+\mathbf{t_2}) && \alpha u_{2z}w_1(\mathbf{R}+\mathbf{t_1}) \\
& && -\beta u_{2x}v_1(\mathbf{R}+\mathbf{t_2}) && -\beta u_{2z}v_1(\mathbf{R}+\mathbf{t_1}) \\
& -u_{2x}w_2(\mathbf{R}) && \alpha u_{2y}w_2(\mathbf{R}+\mathbf{t_2}) && -\alpha u_{2z}w_2(\mathbf{R}+\mathbf{t_1}) \\
& && -\beta u_{2y}v_2(\mathbf{R}+\mathbf{t_2}) && -\beta u_{2z}v_2(\mathbf{R}+\mathbf{t_1}) \\
& -u_{3y}w_1(\mathbf{R}+\mathbf{t_2}) && -\alpha u_{3x}w_1(\mathbf{R}+\mathbf{t_1}+\mathbf{t_2}) && -\alpha u_{3z}w_1(\mathbf{R}+\mathbf{t_1}+\mathbf{t_2}-\mathbf{t_3}) \\
& && -\beta u_{3x}v_1(\mathbf{R}+\mathbf{t_1}+\mathbf{t_2}) && \beta u_{3z}v_1(\mathbf{R}+\mathbf{t_1}+\mathbf{t_2}-\mathbf{t_3}) \\
& -u_{3x}w_2(\mathbf{R}+\mathbf{t_1}+\mathbf{t_2}-\mathbf{t_3}) && -\alpha u_{3y}w_2(\mathbf{R}+\mathbf{t_2}) && \alpha u_{3z}w_2(\mathbf{R}+\mathbf{t_2}-\mathbf{t_3}) \\
& && \beta u_{3y}v_2(\mathbf{R}+\mathbf{t_2}) && \beta u_{3z}v_2(\mathbf{R}+\mathbf{t_2}-\mathbf{t_3}) \\
& u_{4y}w_1(\mathbf{R}+\mathbf{t_1}) && -\alpha u_{4z}w_1(\mathbf{R}+\mathbf{t_1}+\mathbf{t_2}) && \alpha u_{4x}w_1(\mathbf{R}+\mathbf{t_1}+\mathbf{t_2}-\mathbf{t_3}) \\
& && \beta u_{4z}v_1(\mathbf{R}+\mathbf{t_1}+\mathbf{t_2}) && \beta u_{4x}v_1(\mathbf{R}+\mathbf{t_1}+\mathbf{t_2}-\mathbf{t_3}) \\
& u_{4x}w_2(\mathbf{R}+\mathbf{t_1}+\mathbf{t_2}-\mathbf{t_3}) && \alpha u_{4z}w_2(\mathbf{R}+\mathbf{t_1}) && \alpha u_{4y}w_2(\mathbf{R}+\mathbf{t_1}-\mathbf{t_3}) \\
& && \beta u_{4z}v_2(\mathbf{R}+\mathbf{t_1}) && -\beta u_{4y}v_2(\mathbf{R}+\mathbf{t_1}-\mathbf{t_3}))\Big)
\end{aligned}
$$

$$
\begin{aligned}
C_{3xv2}\Big(& -u_{1y}v_1(\mathbf{R}+\mathbf{t_1}) & \alpha u_{1z}v_1(\mathbf{R}+\mathbf{t_1}+\mathbf{t_2}-\mathbf{t_3}) & \quad \alpha u_{1x}v_1(\mathbf{R}+\mathbf{t_2}) \\
& & \beta u_{1z}w_1(\mathbf{R}+\mathbf{t_1}+\mathbf{t_2}-\mathbf{t_3}) & \quad -\beta u_{1x}w_1(\mathbf{R}+\mathbf{t_2}) \\
& -u_{1x}v_2(\mathbf{R}+\mathbf{t_1}-\mathbf{t_3}) & \alpha u_{1z}v_2(\mathbf{R}) & \quad \alpha u_{1y}v_2(\mathbf{R}+\mathbf{t_2}-\mathbf{t_3}) \\
& & -\beta u_{1z}w_2(\mathbf{R}) & \quad \beta u_{1y}w_2(\mathbf{R}+\mathbf{t_2}-\mathbf{t_3}) \\
& u_{2y}v_1(\mathbf{R}+\mathbf{t_2}) & -\alpha u_{2x}v_1(\mathbf{R}+\mathbf{t_1}) & \quad \alpha u_{2z}v_1(\mathbf{R}+\mathbf{t_1}+\mathbf{t_2}) \\
& & \beta u_{2x}w_1(\mathbf{R}+\mathbf{t_1}) & \quad \beta u_{2z}w_1(\mathbf{R}+\mathbf{t_1}+\mathbf{t_2}) \\
& u_{2x}v_2(\mathbf{R}+\mathbf{t_2}) & -\alpha u_{2y}v_2(\mathbf{R}+\mathbf{t_1}) & \quad \alpha u_{2z}v_2(\mathbf{R}) \\
& & -\beta u_{2y}w_2(\mathbf{R}+\mathbf{t_1}) & \quad -\beta u_{2z}w_2(\mathbf{R}) \\
& -u_{3y}v_1(\mathbf{R}+\mathbf{t_1}+\mathbf{t_2}) & -\alpha u_{3z}v_1(\mathbf{R}+\mathbf{t_2}) & \quad -\alpha u_{3x}v_1(\mathbf{R}+\mathbf{t_1}+\mathbf{t_2}-\mathbf{t_3}) \\
& & -\beta u_{3z}w_1(\mathbf{R}+\mathbf{t_2}) & \quad \beta u_{3x}w_1(\mathbf{R}+\mathbf{t_1}+\mathbf{t_2}-\mathbf{t_3}) \\
& u_{3x}v_2(\mathbf{R}+\mathbf{t_2}) & -\alpha u_{3z}v_2(\mathbf{R}+\mathbf{t_1}+\mathbf{t_2}-\mathbf{t_3}) & \quad \alpha u_{3y}v_2(\mathbf{R}+\mathbf{t_2}-\mathbf{t_3}) \\
& & \beta u_{3z}w_2(\mathbf{R}+\mathbf{t_1}+\mathbf{t_2}-\mathbf{t_3}) & \quad \beta u_{3y}w_2(\mathbf{R}+\mathbf{t_2}-\mathbf{t_3}) \\
& u_{4y}v_1(\mathbf{R}+\mathbf{t_1}+\mathbf{t_2}-\mathbf{t_3}) & \alpha u_{4x}v_1(\mathbf{R}+\mathbf{t_1}+\mathbf{t_2}) & \quad -\alpha u_{4z}v_1(\mathbf{R}+\mathbf{t_1}) \\
& & -\beta u_{4x}w_1(\mathbf{R}+\mathbf{t_1}+\mathbf{t_2}) & \quad -\beta u_{4z}w_1(\mathbf{R}+\mathbf{t_1}) \\
& -u_{4x}v_2(\mathbf{R}+\mathbf{t_1}-\mathbf{t_3}) & -\alpha u_{4y}v_2(\mathbf{R}+\mathbf{t_1}) & \quad -\alpha u_{4z}v_2(\mathbf{R}+\mathbf{t_1}+\mathbf{t_2}-\mathbf{t_3}) \\
& & -\beta u_{4y}w_2(\mathbf{R}+\mathbf{t_1}) & \quad \beta u_{4z}w_2(\mathbf{R}+\mathbf{t_1}+\mathbf{t_2}-\mathbf{t_3}) \\
& -\big(u_{1x}v_1(\mathbf{R}+\mathbf{t_2}) & -\alpha u_{1y}v_1(\mathbf{R}+\mathbf{t_1}) & \quad -\alpha u_{1z}v_1(\mathbf{R}+\mathbf{t_1}+\mathbf{t_2}-\mathbf{t_3}) \\
& & -\beta u_{1y}w_1(\mathbf{R}+\mathbf{t_1}) & \quad \beta u_{1z}w_1(\mathbf{R}+\mathbf{t_1}+\mathbf{t_2}-\mathbf{t_3}) \\
& u_{1y}v_2(\mathbf{R}+\mathbf{t_2}-\mathbf{t_3}) & -\alpha u_{1x}v_2(\mathbf{R}+\mathbf{t_1}-\mathbf{t_3}) & \quad -\alpha u_{1z}v_2(\mathbf{R}) \\
& & \beta u_{1x}w_2(\mathbf{R}+\mathbf{t_1}-\mathbf{t_3}) & \quad -\beta u_{1z}w_2(\mathbf{R}) \\
& -u_{2x}v_1(\mathbf{R}+\mathbf{t_1}) & -\alpha u_{2z}v_1(\mathbf{R}+\mathbf{t_1}+\mathbf{t_2}) & \quad \alpha u_{2y}v_1(\mathbf{R}+\mathbf{t_2}) \\
& & \beta u_{2z}w_1(\mathbf{R}+\mathbf{t_1}+\mathbf{t_2}) & \quad \beta u_{2y}w_1(\mathbf{R}+\mathbf{t_2}) \\
& -u_{2y}v_2(\mathbf{R}+\mathbf{t_1}) & -\alpha u_{2z}v_2(\mathbf{R}) & \quad \alpha u_{2x}v_2(\mathbf{R}+\mathbf{t_2}) \\
& & -\beta u_{2z}w_2(\mathbf{R}) & \quad -\beta u_{2x}w_2(\mathbf{R}+\mathbf{t_2}) \\
& -u_{3x}v_1(\mathbf{R}+\mathbf{t_1}+\mathbf{t_2}-\mathbf{t_3}) & -\alpha u_{3y}v_1(\mathbf{R}+\mathbf{t_1}+\mathbf{t_2}) & \quad \alpha u_{3z}v_1(\mathbf{R}+\mathbf{t_2}) \\
& & -\beta u_{3y}w_1(\mathbf{R}+\mathbf{t_1}+\mathbf{t_2}) & \quad -\beta u_{3z}w_1(\mathbf{R}+\mathbf{t_2}) \\
& u_{3y}v_2(\mathbf{R}+\mathbf{t_2}-\mathbf{t_3}) & \alpha u_{3x}v_2(\mathbf{R}+\mathbf{t_2}) & \quad \alpha u_{3z}v_2(\mathbf{R}+\mathbf{t_1}+\mathbf{t_2}-\mathbf{t_3}) \\
& & -\beta u_{3x}w_2(\mathbf{R}+\mathbf{t_2}) & \quad \beta u_{3z}w_2(\mathbf{R}+\mathbf{t_1}+\mathbf{t_2}-\mathbf{t_3}) \\
& u_{4x}v_1(\mathbf{R}+\mathbf{t_1}+\mathbf{t_2}) & \alpha u_{4z}v_1(\mathbf{R}+\mathbf{t_1}) & \quad \alpha u_{4y}v_1(\mathbf{R}+\mathbf{t_1}+\mathbf{t_2}-\mathbf{t_3}) \\
& & -\beta u_{4z}w_1(\mathbf{R}+\mathbf{t_1}) & \quad \beta u_{4y}w_1(\mathbf{R}+\mathbf{t_1}+\mathbf{t_2}-\mathbf{t_3}) \\
& -u_{4y}v_2(\mathbf{R}+\mathbf{t_1}) & \alpha u_{4z}v_2(\mathbf{R}+\mathbf{t_1}+\mathbf{t_2}-\mathbf{t_3}) & \quad -\alpha u_{4x}v_2(\mathbf{R}+\mathbf{t_1}-\mathbf{t_3}) \\
& & \beta u_{4z}w_2(\mathbf{R}+\mathbf{t_1}+\mathbf{t_2}-\mathbf{t_3}) & \quad \beta u_{4x}w_2(\mathbf{R}+\mathbf{t_1}-\mathbf{t_3}))\Big)
\end{aligned}
$$

$$
\begin{aligned}
C_{3xw2}\Big(& u_{1y}w_1(\mathbf{R}+\mathbf{t_1}) && -\alpha u_{1z}w_1(\mathbf{R}+\mathbf{t_1}+\mathbf{t_2}-\mathbf{t_3}) && -\alpha u_{1x}w_1(\mathbf{R}+\mathbf{t_2}) \\
& && \beta u_{1z}v_1(\mathbf{R}+\mathbf{t_1}+\mathbf{t_2}-\mathbf{t_3}) && -\beta u_{1x}v_1(\mathbf{R}+\mathbf{t_2}) \\
& -u_{1x}w_2(\mathbf{R}+\mathbf{t_1}-\mathbf{t_3}) && \alpha u_{1z}w_2(\mathbf{R}) && \alpha u_{1y}w_2(\mathbf{R}+\mathbf{t_2}-\mathbf{t_3}) \\
& && \beta u_{1z}v_2(\mathbf{R}) && -\beta u_{1y}v_2(\mathbf{R}+\mathbf{t_2}-\mathbf{t_3}) \\
& -u_{2y}w_1(\mathbf{R}+\mathbf{t_2}) && \alpha u_{2x}w_1(\mathbf{R}+\mathbf{t_1}) && -\alpha u_{2z}w_1(\mathbf{R}+\mathbf{t_1}+\mathbf{t_2}) \\
& && \beta u_{2x}v_1(\mathbf{R}+\mathbf{t_1}) && \beta u_{2z}v_1(\mathbf{R}+\mathbf{t_1}+\mathbf{t_2}) \\
& u_{2x}w_2(\mathbf{R}+\mathbf{t_2}) && -\alpha u_{2y}w_2(\mathbf{R}+\mathbf{t_1}) && \alpha u_{2z}w_2(\mathbf{R}) \\
& && \beta u_{2y}v_2(\mathbf{R}+\mathbf{t_1}) && \beta u_{2z}v_2(\mathbf{R}) \\
& u_{3y}w_1(\mathbf{R}+\mathbf{t_1}+\mathbf{t_2}) && \alpha u_{3z}w_1(\mathbf{R}+\mathbf{t_2}) && \alpha u_{3x}w_1(\mathbf{R}+\mathbf{t_1}+\mathbf{t_2}-\mathbf{t_3}) \\
& && -\beta u_{3z}v_1(\mathbf{R}+\mathbf{t_2}) && \beta u_{3x}v_1(\mathbf{R}+\mathbf{t_1}+\mathbf{t_2}-\mathbf{t_3}) \\
& u_{3x}w_2(\mathbf{R}+\mathbf{t_2}) && -\alpha u_{3z}w_2(\mathbf{R}+\mathbf{t_1}+\mathbf{t_2}-\mathbf{t_3}) && \alpha u_{3y}w_2(\mathbf{R}+\mathbf{t_2}-\mathbf{t_3}) \\
& && -\beta u_{3z}v_2(\mathbf{R}+\mathbf{t_1}+\mathbf{t_2}-\mathbf{t_3}) && -\beta u_{3y}v_2(\mathbf{R}+\mathbf{t_2}-\mathbf{t_3}) \\
& -u_{4y}w_1(\mathbf{R}+\mathbf{t_1}+\mathbf{t_2}-\mathbf{t_3}) && -\alpha u_{4x}w_1(\mathbf{R}+\mathbf{t_1}+\mathbf{t_2}) && \alpha u_{4z}w_1(\mathbf{R}+\mathbf{t_1}) \\
& && -\beta u_{4x}v_1(\mathbf{R}+\mathbf{t_1}+\mathbf{t_2}) && -\beta u_{4z}v_1(\mathbf{R}+\mathbf{t_1}) \\
& -u_{4x}w_2(\mathbf{R}+\mathbf{t_1}-\mathbf{t_3}) && -\alpha u_{4y}w_2(\mathbf{R}+\mathbf{t_1}) && -\alpha u_{4z}w_2(\mathbf{R}+\mathbf{t_1}+\mathbf{t_2}-\mathbf{t_3}) \\
& && \beta u_{4y}v_2(\mathbf{R}+\mathbf{t_1}) && -\beta u_{4z}v_2(\mathbf{R}+\mathbf{t_1}+\mathbf{t_2}-\mathbf{t_3}) \\
& \big(u_{1x}w_1(\mathbf{R}+\mathbf{t_2}) && -\alpha u_{1y}w_1(\mathbf{R}+\mathbf{t_1}) && -\alpha u_{1z}w_1(\mathbf{R}+\mathbf{t_1}+\mathbf{t_2}-\mathbf{t_3}) \\
& && \beta u_{1y}v_1(\mathbf{R}+\mathbf{t_1}) && -\beta u_{1z}v_1(\mathbf{R}+\mathbf{t_1}+\mathbf{t_2}-\mathbf{t_3}) \\
& -u_{1y}w_2(\mathbf{R}+\mathbf{t_2}-\mathbf{t_3}) && \alpha u_{1x}w_2(\mathbf{R}+\mathbf{t_1}-\mathbf{t_3}) && \alpha u_{1z}w_2(\mathbf{R}) \\
& && \beta u_{1x}v_2(\mathbf{R}+\mathbf{t_1}-\mathbf{t_3}) && -\beta u_{1z}v_2(\mathbf{R}) \\
& -u_{2x}w_1(\mathbf{R}+\mathbf{t_1}) && -\alpha u_{2z}w_1(\mathbf{R}+\mathbf{t_1}+\mathbf{t_2}) && \alpha u_{2y}w_1(\mathbf{R}+\mathbf{t_2}) \\
& && -\beta u_{2z}v_1(\mathbf{R}+\mathbf{t_1}+\mathbf{t_2}) && -\beta u_{2y}v_1(\mathbf{R}+\mathbf{t_2}) \\
& u_{2y}w_2(\mathbf{R}+\mathbf{t_1}) && \alpha u_{2z}w_2(\mathbf{R}) && -\alpha u_{2x}w_2(\mathbf{R}+\mathbf{t_2}) \\
& && -\beta u_{2z}v_2(\mathbf{R}) && -\beta u_{2x}v_2(\mathbf{R}+\mathbf{t_2}) \\
& -u_{3x}w_1(\mathbf{R}+\mathbf{t_1}+\mathbf{t_2}-\mathbf{t_3}) && -\alpha u_{3y}w_1(\mathbf{R}+\mathbf{t_1}+\mathbf{t_2}) && \alpha u_{3z}w_1(\mathbf{R}+\mathbf{t_2}) \\
& && \beta u_{3y}v_1(\mathbf{R}+\mathbf{t_1}+\mathbf{t_2}) && \beta u_{3z}v_1(\mathbf{R}+\mathbf{t_2}) \\
& -u_{3y}w_2(\mathbf{R}+\mathbf{t_2}-\mathbf{t_3}) && -\alpha u_{3x}w_2(\mathbf{R}+\mathbf{t_2}) && -\alpha u_{3z}w_2(\mathbf{R}+\mathbf{t_1}+\mathbf{t_2}-\mathbf{t_3}) \\
& && -\beta u_{3x}v_2(\mathbf{R}+\mathbf{t_2}) && \beta u_{3z}v_2(\mathbf{R}+\mathbf{t_1}+\mathbf{t_2}-\mathbf{t_3}) \\
& u_{4x}w_1(\mathbf{R}+\mathbf{t_1}+\mathbf{t_2}) && \alpha u_{4z}w_1(\mathbf{R}+\mathbf{t_1}) && \alpha u_{4y}w_1(\mathbf{R}+\mathbf{t_1}+\mathbf{t_2}-\mathbf{t_3}) \\
& && \beta u_{4z}v_1(\mathbf{R}+\mathbf{t_1}) && -\beta u_{4y}v_1(\mathbf{R}+\mathbf{t_1}+\mathbf{t_2}-\mathbf{t_3}) \\
& u_{4y}w_2(\mathbf{R}+\mathbf{t_1}) && -\alpha u_{4z}w_2(\mathbf{R}+\mathbf{t_1}+\mathbf{t_2}-\mathbf{t_3}) && \alpha u_{4x}w_2(\mathbf{R}+\mathbf{t_1}-\mathbf{t_3}) \\
& && \beta u_{4z}v_2(\mathbf{R}+\mathbf{t_1}+\mathbf{t_2}-\mathbf{t_3}) && \beta u_{4x}v_2(\mathbf{R}+\mathbf{t_1}-\mathbf{t_3})\big)\Big)
\end{aligned}
$$

$$
\begin{aligned}
C_{3yv2}\Big(& u_{1x}v_1(\mathbf{R}+\mathbf{t_1}) && -\alpha u_{1y}v_1(\mathbf{R}+\mathbf{t_1}+\mathbf{t_2}-\mathbf{t_3}) && -\alpha u_{1z}v_1(\mathbf{R}+\mathbf{t_2}) \\
& && -\beta u_{1y}w_1(\mathbf{R}+\mathbf{t_1}+\mathbf{t_2}-\mathbf{t_3}) && \beta u_{1z}w_1(\mathbf{R}+\mathbf{t_2}) \\
& u_{1y}v_2(\mathbf{R}+\mathbf{t_1}-\mathbf{t_3}) && -\alpha u_{1x}v_2(\mathbf{R}) && -\alpha u_{1z}v_2(\mathbf{R}+\mathbf{t_2}-\mathbf{t_3}) \\
& && \beta u_{1x}w_2(\mathbf{R}) && -\beta u_{1z}w_2(\mathbf{R}+\mathbf{t_2}-\mathbf{t_3}) \\
& -u_{2x}v_1(\mathbf{R}+\mathbf{t_2}) && -\alpha u_{2z}v_1(\mathbf{R}+\mathbf{t_1}) && \alpha u_{2y}v_1(\mathbf{R}+\mathbf{t_1}+\mathbf{t_2}) \\
& && \beta u_{2z}w_1(\mathbf{R}+\mathbf{t_1}) && \beta u_{2y}w_1(\mathbf{R}+\mathbf{t_1}+\mathbf{t_2}) \\
& -u_{2y}v_2(\mathbf{R}+\mathbf{t_2}) && -\alpha u_{2z}v_2(\mathbf{R}+\mathbf{t_1}) && \alpha u_{2x}v_2(\mathbf{R}) \\
& && -\beta u_{2z}w_2(\mathbf{R}+\mathbf{t_1}) && -\beta u_{2x}w_2(\mathbf{R}) \\
& -u_{3x}v_1(\mathbf{R}+\mathbf{t_1}+\mathbf{t_2}) && -\alpha u_{3y}v_1(\mathbf{R}+\mathbf{t_2}) && \alpha u_{3z}v_1(\mathbf{R}+\mathbf{t_1}+\mathbf{t_2}-\mathbf{t_3}) \\
& && -\beta u_{3y}w_1(\mathbf{R}+\mathbf{t_2}) && -\beta u_{3z}w_1(\mathbf{R}+\mathbf{t_1}+\mathbf{t_2}-\mathbf{t_3}) \\
& u_{3y}v_2(\mathbf{R}+\mathbf{t_2}) && \alpha u_{3x}v_2(\mathbf{R}+\mathbf{t_1}+\mathbf{t_2}-\mathbf{t_3}) && \alpha u_{3z}v_2(\mathbf{R}+\mathbf{t_2}-\mathbf{t_3}) \\
& && -\beta u_{3x}w_2(\mathbf{R}+\mathbf{t_1}+\mathbf{t_2}-\mathbf{t_3}) && \beta u_{3z}w_2(\mathbf{R}+\mathbf{t_2}-\mathbf{t_3}) \\
& u_{4x}v_1(\mathbf{R}+\mathbf{t_1}+\mathbf{t_2}-\mathbf{t_3}) && \alpha u_{4z}v_1(\mathbf{R}+\mathbf{t_1}+\mathbf{t_2}) && \alpha u_{4y}v_1(\mathbf{R}+\mathbf{t_1}) \\
& && -\beta u_{4z}w_1(\mathbf{R}+\mathbf{t_1}+\mathbf{t_2}) && \beta u_{4y}w_1(\mathbf{R}+\mathbf{t_1}) \\
& -u_{4y}v_2(\mathbf{R}+\mathbf{t_1}-\mathbf{t_3}) && \alpha u_{4z}v_2(\mathbf{R}+\mathbf{t_1}) && -\alpha u_{4x}v_2(\mathbf{R}+\mathbf{t_1}+\mathbf{t_2}-\mathbf{t_3}) \\
& && \beta u_{4z}w_2(\mathbf{R}+\mathbf{t_1}) && \beta u_{4x}w_2(\mathbf{R}+\mathbf{t_1}+\mathbf{t_2}-\mathbf{t_3}) \\
& -\big(-u_{1y}v_1(\mathbf{R}+\mathbf{t_2}) && \alpha u_{1z}v_1(\mathbf{R}+\mathbf{t_1}) && \alpha u_{1x}v_1(\mathbf{R}+\mathbf{t_1}+\mathbf{t_2}-\mathbf{t_3}) \\
& && \beta u_{1z}w_1(\mathbf{R}+\mathbf{t_1}) && -\beta u_{1x}w_1(\mathbf{R}+\mathbf{t_1}+\mathbf{t_2}-\mathbf{t_3}) \\
& -u_{1x}v_2(\mathbf{R}+\mathbf{t_2}-\mathbf{t_3}) && \alpha u_{1z}v_2(\mathbf{R}+\mathbf{t_1}-\mathbf{t_3}) && \alpha u_{1y}v_2(\mathbf{R}) \\
& && -\beta u_{1z}w_2(\mathbf{R}+\mathbf{t_1}-\mathbf{t_3}) && \beta u_{1y}w_2(\mathbf{R}) \\
& u_{2y}v_1(\mathbf{R}+\mathbf{t_1}) && -\alpha u_{2x}v_1(\mathbf{R}+\mathbf{t_1}+\mathbf{t_2}) && \alpha u_{2z}v_1(\mathbf{R}+\mathbf{t_2}) \\
& && \beta u_{2x}w_1(\mathbf{R}+\mathbf{t_1}+\mathbf{t_2}) && \beta u_{2z}w_1(\mathbf{R}+\mathbf{t_2}) \\
& u_{2x}v_2(\mathbf{R}+\mathbf{t_1}) && -\alpha u_{2y}v_2(\mathbf{R}) && \alpha u_{2z}v_2(\mathbf{R}+\mathbf{t_2}) \\
& && -\beta u_{2y}w_2(\mathbf{R}) && -\beta u_{2z}w_2(\mathbf{R}+\mathbf{t_2}) \\
& -u_{3y}v_1(\mathbf{R}+\mathbf{t_1}+\mathbf{t_2}-\mathbf{t_3}) && -\alpha u_{3z}v_1(\mathbf{R}+\mathbf{t_1}+\mathbf{t_2}) && -\alpha u_{3x}v_1(\mathbf{R}+\mathbf{t_2}) \\
& && -\beta u_{3z}w_1(\mathbf{R}+\mathbf{t_1}+\mathbf{t_2}) && \beta u_{3x}w_1(\mathbf{R}+\mathbf{t_2}) \\
& u_{3x}v_2(\mathbf{R}+\mathbf{t_2}-\mathbf{t_3}) && -\alpha u_{3z}v_2(\mathbf{R}+\mathbf{t_2}) && \alpha u_{3y}v_2(\mathbf{R}+\mathbf{t_1}+\mathbf{t_2}-\mathbf{t_3}) \\
& && \beta u_{3z}w_2(\mathbf{R}+\mathbf{t_2}) && \beta u_{3y}w_2(\mathbf{R}+\mathbf{t_1}+\mathbf{t_2}-\mathbf{t_3}) \\
& u_{4y}v_1(\mathbf{R}+\mathbf{t_1}+\mathbf{t_2}) && \alpha u_{4x}v_1(\mathbf{R}+\mathbf{t_1}) && -\alpha u_{4z}v_1(\mathbf{R}+\mathbf{t_1}+\mathbf{t_2}-\mathbf{t_3}) \\
& && -\beta u_{4x}w_1(\mathbf{R}+\mathbf{t_1}) && -\beta u_{4z}w_1(\mathbf{R}+\mathbf{t_1}+\mathbf{t_2}-\mathbf{t_3}) \\
& -u_{4x}v_2(\mathbf{R}+\mathbf{t_1}) && -\alpha u_{4y}v_2(\mathbf{R}+\mathbf{t_1}+\mathbf{t_2}-\mathbf{t_3}) && -\alpha u_{4z}v_2(\mathbf{R}+\mathbf{t_1}-\mathbf{t_3}) \\
& && -\beta u_{4y}w_2(\mathbf{R}+\mathbf{t_1}+\mathbf{t_2}-\mathbf{t_3}) && \beta u_{4z}w_2(\mathbf{R}+\mathbf{t_1}-\mathbf{t_3}))\Big)
\end{aligned}
$$

$$
\begin{aligned}
C_{3yw2}\Big(& -u_{1x}w_1(\mathbf{R}+\mathbf{t_1}) & \alpha u_{1y}w_1(\mathbf{R}+\mathbf{t_1}+\mathbf{t_2}-\mathbf{t_3}) & \alpha u_{1z}w_1(\mathbf{R}+\mathbf{t_2}) \\
& & -\beta u_{1y}v_1(\mathbf{R}+\mathbf{t_1}+\mathbf{t_2}-\mathbf{t_3}) & \beta u_{1z}v_1(\mathbf{R}+\mathbf{t_2}) \\
& u_{1y}w_2(\mathbf{R}+\mathbf{t_1}-\mathbf{t_3}) & -\alpha u_{1x}w_2(\mathbf{R}) & -\alpha u_{1z}w_2(\mathbf{R}+\mathbf{t_2}-\mathbf{t_3}) \\
& & -\beta u_{1x}v_2(\mathbf{R}) & \beta u_{1z}v_2(\mathbf{R}+\mathbf{t_2}-\mathbf{t_3}) \\
& u_{2x}w_1(\mathbf{R}+\mathbf{t_2}) & \alpha u_{2z}w_1(\mathbf{R}+\mathbf{t_1}) & -\alpha u_{2y}w_1(\mathbf{R}+\mathbf{t_1}+\mathbf{t_2}) \\
& & \beta u_{2z}v_1(\mathbf{R}+\mathbf{t_1}) & \beta u_{2y}v_1(\mathbf{R}+\mathbf{t_1}+\mathbf{t_2}) \\
& -u_{2y}w_2(\mathbf{R}+\mathbf{t_2}) & -\alpha u_{2z}w_2(\mathbf{R}+\mathbf{t_1}) & \alpha u_{2x}w_2(\mathbf{R}) \\
& & \beta u_{2z}v_2(\mathbf{R}+\mathbf{t_1}) & \beta u_{2x}v_2(\mathbf{R}) \\
& u_{3x}w_1(\mathbf{R}+\mathbf{t_1}+\mathbf{t_2}) & \alpha u_{3y}w_1(\mathbf{R}+\mathbf{t_2}) & -\alpha u_{3z}w_1(\mathbf{R}+\mathbf{t_1}+\mathbf{t_2}-\mathbf{t_3}) \\
& & -\beta u_{3y}v_1(\mathbf{R}+\mathbf{t_2}) & -\beta u_{3z}v_1(\mathbf{R}+\mathbf{t_1}+\mathbf{t_2}-\mathbf{t_3}) \\
& u_{3y}w_2(\mathbf{R}+\mathbf{t_2}) & \alpha u_{3x}w_2(\mathbf{R}+\mathbf{t_1}+\mathbf{t_2}-\mathbf{t_3}) & \alpha u_{3z}w_2(\mathbf{R}+\mathbf{t_2}-\mathbf{t_3}) \\
& & \beta u_{3x}v_2(\mathbf{R}+\mathbf{t_1}+\mathbf{t_2}-\mathbf{t_3}) & -\beta u_{3z}v_2(\mathbf{R}+\mathbf{t_2}-\mathbf{t_3}) \\
& -u_{4x}w_1(\mathbf{R}+\mathbf{t_1}+\mathbf{t_2}-\mathbf{t_3}) & -\alpha u_{4z}w_1(\mathbf{R}+\mathbf{t_1}+\mathbf{t_2}) & -\alpha u_{4y}w_1(\mathbf{R}+\mathbf{t_1}) \\
& & -\beta u_{4z}v_1(\mathbf{R}+\mathbf{t_1}+\mathbf{t_2}) & \beta u_{4y}v_1(\mathbf{R}+\mathbf{t_1}) \\
& -u_{4y}w_2(\mathbf{R}+\mathbf{t_1}-\mathbf{t_3}) & \alpha u_{4z}w_2(\mathbf{R}+\mathbf{t_1}) & -\alpha u_{4x}w_2(\mathbf{R}+\mathbf{t_1}+\mathbf{t_2}-\mathbf{t_3}) \\
& & -\beta u_{4z}v_2(\mathbf{R}+\mathbf{t_1}) & -\beta u_{4x}v_2(\mathbf{R}+\mathbf{t_1}+\mathbf{t_2}-\mathbf{t_3}) \\
& \big(-u_{1y}w_1(\mathbf{R}+\mathbf{t_2}) & \alpha u_{1z}w_1(\mathbf{R}+\mathbf{t_1}) & \alpha u_{1x}w_1(\mathbf{R}+\mathbf{t_1}+\mathbf{t_2}-\mathbf{t_3}) \\
& & -\beta u_{1z}v_1(\mathbf{R}+\mathbf{t_1}) & \beta u_{1x}v_1(\mathbf{R}+\mathbf{t_1}+\mathbf{t_2}-\mathbf{t_3}) \\
& u_{1x}w_2(\mathbf{R}+\mathbf{t_2}-\mathbf{t_3}) & -\alpha u_{1z}w_2(\mathbf{R}+\mathbf{t_1}-\mathbf{t_3}) & -\alpha u_{1y}w_2(\mathbf{R}) \\
& & -\beta u_{1z}v_2(\mathbf{R}+\mathbf{t_1}-\mathbf{t_3}) & \beta u_{1y}v_2(\mathbf{R}) \\
& u_{2y}w_1(\mathbf{R}+\mathbf{t_1}) & -\alpha u_{2x}w_1(\mathbf{R}+\mathbf{t_1}+\mathbf{t_2}) & \alpha u_{2z}w_1(\mathbf{R}+\mathbf{t_2}) \\
& & -\beta u_{2x}v_1(\mathbf{R}+\mathbf{t_1}+\mathbf{t_2}) & -\beta u_{2z}v_1(\mathbf{R}+\mathbf{t_2}) \\
& -u_{2x}w_2(\mathbf{R}+\mathbf{t_1}) & \alpha u_{2y}w_2(\mathbf{R}) & -\alpha u_{2z}w_2(\mathbf{R}+\mathbf{t_2}) \\
& & -\beta u_{2y}v_2(\mathbf{R}) & -\beta u_{2z}v_2(\mathbf{R}+\mathbf{t_2}) \\
& -u_{3y}w_1(\mathbf{R}+\mathbf{t_1}+\mathbf{t_2}-\mathbf{t_3}) & -\alpha u_{3z}w_1(\mathbf{R}+\mathbf{t_1}+\mathbf{t_2}) & -\alpha u_{3x}w_1(\mathbf{R}+\mathbf{t_2}) \\
& & \beta u_{3z}v_1(\mathbf{R}+\mathbf{t_1}+\mathbf{t_2}) & -\beta u_{3x}v_1(\mathbf{R}+\mathbf{t_2}) \\
& -u_{3x}w_2(\mathbf{R}+\mathbf{t_2}-\mathbf{t_3}) & \alpha u_{3z}w_2(\mathbf{R}+\mathbf{t_2}) & -\alpha u_{3y}w_2(\mathbf{R}+\mathbf{t_1}+\mathbf{t_2}-\mathbf{t_3}) \\
& & \beta u_{3z}v_2(\mathbf{R}+\mathbf{t_2}) & \beta u_{3y}v_2(\mathbf{R}+\mathbf{t_1}+\mathbf{t_2}-\mathbf{t_3}) \\
& u_{4y}w_1(\mathbf{R}+\mathbf{t_1}+\mathbf{t_2}) & \alpha u_{4x}w_1(\mathbf{R}+\mathbf{t_1}) & -\alpha u_{4z}w_1(\mathbf{R}+\mathbf{t_1}+\mathbf{t_2}-\mathbf{t_3}) \\
& & \beta u_{4x}v_1(\mathbf{R}+\mathbf{t_1}) & \beta u_{4z}v_1(\mathbf{R}+\mathbf{t_1}+\mathbf{t_2}-\mathbf{t_3}) \\
& u_{4x}w_2(\mathbf{R}+\mathbf{t_1}) & \alpha u_{4y}w_2(\mathbf{R}+\mathbf{t_1}+\mathbf{t_2}-\mathbf{t_3}) & \alpha u_{4z}w_2(\mathbf{R}+\mathbf{t_1}-\mathbf{t_3}) \\
& & -\beta u_{4y}v_2(\mathbf{R}+\mathbf{t_1}+\mathbf{t_2}-\mathbf{t_3}) & \beta u_{4z}v_2(\mathbf{R}+\mathbf{t_1}-\mathbf{t_3}))\Big)
\end{aligned}
$$

$$
\begin{aligned}
C_{3zv1}\Big(& -u_{1z}v_1(\mathbf{R}+\mathbf{t_1}+\mathbf{t_2}-\mathbf{t_3}) & \alpha u_{1y}v_1(\mathbf{R}+\mathbf{t_1}) & \quad \alpha u_{1x}v_1(\mathbf{R}+\mathbf{t_2}) \\
& & -\beta u_{1y}w_1(\mathbf{R}+\mathbf{t_1}) & \quad \beta u_{1x}w_1(\mathbf{R}+\mathbf{t_2}) \\
& -u_{1z}v_2(\mathbf{R}) & \alpha u_{1y}v_2(\mathbf{R}+\mathbf{t_2}-\mathbf{t_3}) & \quad \alpha u_{1x}v_2(\mathbf{R}+\mathbf{t_1}-\mathbf{t_3}) \\
& & -\beta u_{1y}w_2(\mathbf{R}+\mathbf{t_2}-\mathbf{t_3}) & \quad \beta u_{1x}w_2(\mathbf{R}+\mathbf{t_1}-\mathbf{t_3}) \\
& -u_{2z}v_1(\mathbf{R}+\mathbf{t_1}+\mathbf{t_2}) & -\alpha u_{2x}v_1(\mathbf{R}+\mathbf{t_1}) & \quad -\alpha u_{2y}v_1(\mathbf{R}+\mathbf{t_2}) \\
& & -\beta u_{2x}w_1(\mathbf{R}+\mathbf{t_1}) & \quad \beta u_{2y}w_1(\mathbf{R}+\mathbf{t_2}) \\
& -u_{2z}v_2(\mathbf{R}) & -\alpha u_{2y}v_2(\mathbf{R}+\mathbf{t_1}) & \quad -\alpha u_{2x}v_2(\mathbf{R}+\mathbf{t_2}) \\
& & \beta u_{2y}w_2(\mathbf{R}+\mathbf{t_1}) & \quad -\beta u_{2x}w_2(\mathbf{R}+\mathbf{t_2}) \\
& u_{3z}v_1(\mathbf{R}+\mathbf{t_2}) & \alpha u_{3y}v_1(\mathbf{R}+\mathbf{t_1}+\mathbf{t_2}) & \quad -\alpha u_{3x}v_1(\mathbf{R}+\mathbf{t_1}+\mathbf{t_2}-\mathbf{t_3}) \\
& & -\beta u_{3y}w_1(\mathbf{R}+\mathbf{t_1}+\mathbf{t_2}) & \quad -\beta u_{3x}w_1(\mathbf{R}+\mathbf{t_1}+\mathbf{t_2}-\mathbf{t_3}) \\
& u_{3z}v_2(\mathbf{R}+\mathbf{t_1}+\mathbf{t_2}-\mathbf{t_3}) & -\alpha u_{3x}v_2(\mathbf{R}+\mathbf{t_2}) & \quad \alpha u_{3y}v_2(\mathbf{R}+\mathbf{t_2}-\mathbf{t_3}) \\
& & -\beta u_{3x}w_2(\mathbf{R}+\mathbf{t_2}) & \quad -\beta u_{3y}w_2(\mathbf{R}+\mathbf{t_2}-\mathbf{t_3}) \\
& u_{4z}v_1(\mathbf{R}+\mathbf{t_1}) & \alpha u_{4x}v_1(\mathbf{R}+\mathbf{t_1}+\mathbf{t_2}) & \quad -\alpha u_{4y}v_1(\mathbf{R}+\mathbf{t_1}+\mathbf{t_2}-\mathbf{t_3}) \\
& & \beta u_{4x}w_1(\mathbf{R}+\mathbf{t_1}+\mathbf{t_2}) & \quad \beta u_{4y}w_1(\mathbf{R}+\mathbf{t_1}+\mathbf{t_2}-\mathbf{t_3}) \\
& u_{4z}v_2(\mathbf{R}+\mathbf{t_1}+\mathbf{t_2}-\mathbf{t_3}) & -\alpha u_{4y}v_2(\mathbf{R}+\mathbf{t_1}) & \quad \alpha u_{4x}v_2(\mathbf{R}+\mathbf{t_1}-\mathbf{t_3}) \\
& & \beta u_{4y}w_2(\mathbf{R}+\mathbf{t_1}) & \quad \beta u_{4x}w_2(\mathbf{R}+\mathbf{t_1}-\mathbf{t_3}))\Big)
\end{aligned}
$$

$$
\begin{aligned}
C_{3zv2}\Big(& -u_{1z}v_1(\mathbf{R}+\mathbf{t_1}) & \alpha u_{1x}v_1(\mathbf{R}+\mathbf{t_1}+\mathbf{t_2}-\mathbf{t_3}) & \quad \alpha u_{1y}v_1(\mathbf{R}+\mathbf{t_2}) \\
& & \beta u_{1x}w_1(\mathbf{R}+\mathbf{t_1}+\mathbf{t_2}-\mathbf{t_3}) & \quad -\beta u_{1y}w_1(\mathbf{R}+\mathbf{t_2}) \\
& -u_{1z}v_2(\mathbf{R}+\mathbf{t_1}-\mathbf{t_3}) & \alpha u_{1y}v_2(\mathbf{R}) & \quad \alpha u_{1x}v_2(\mathbf{R}+\mathbf{t_2}-\mathbf{t_3}) \\
& & -\beta u_{1y}w_2(\mathbf{R}) & \quad \beta u_{1x}w_2(\mathbf{R}+\mathbf{t_2}-\mathbf{t_3}) \\
& -u_{2z}v_1(\mathbf{R}+\mathbf{t_2}) & -\alpha u_{2y}v_1(\mathbf{R}+\mathbf{t_1}) & \quad -\alpha u_{2x}v_1(\mathbf{R}+\mathbf{t_1}+\mathbf{t_2}) \\
& & \beta u_{2y}w_1(\mathbf{R}+\mathbf{t_1}) & \quad -\beta u_{2x}w_1(\mathbf{R}+\mathbf{t_1}+\mathbf{t_2}) \\
& -u_{2z}v_2(\mathbf{R}+\mathbf{t_2}) & -\alpha u_{2x}v_2(\mathbf{R}+\mathbf{t_1}) & \quad -\alpha u_{2y}v_2(\mathbf{R}) \\
& & -\beta u_{2x}w_2(\mathbf{R}+\mathbf{t_1}) & \quad \beta u_{2y}w_2(\mathbf{R}) \\
& u_{3z}v_1(\mathbf{R}+\mathbf{t_1}+\mathbf{t_2}) & -\alpha u_{3x}v_1(\mathbf{R}+\mathbf{t_2}) & \quad \alpha u_{3y}v_1(\mathbf{R}+\mathbf{t_1}+\mathbf{t_2}-\mathbf{t_3}) \\
& & -\beta u_{3x}w_1(\mathbf{R}+\mathbf{t_2}) & \quad -\beta u_{3y}w_1(\mathbf{R}+\mathbf{t_1}+\mathbf{t_2}-\mathbf{t_3}) \\
& u_{3z}v_2(\mathbf{R}+\mathbf{t_2}) & \alpha u_{3y}v_2(\mathbf{R}+\mathbf{t_1}+\mathbf{t_2}-\mathbf{t_3}) & \quad -\alpha u_{3x}v_2(\mathbf{R}+\mathbf{t_2}-\mathbf{t_3}) \\
& & -\beta u_{3y}w_2(\mathbf{R}+\mathbf{t_1}+\mathbf{t_2}-\mathbf{t_3}) & \quad -\beta u_{3x}w_2(\mathbf{R}+\mathbf{t_2}-\mathbf{t_3}) \\
& u_{4z}v_1(\mathbf{R}+\mathbf{t_1}+\mathbf{t_2}-\mathbf{t_3}) & -\alpha u_{4y}v_1(\mathbf{R}+\mathbf{t_1}+\mathbf{t_2}) & \quad \alpha u_{4x}v_1(\mathbf{R}+\mathbf{t_1}) \\
& & \beta u_{4y}w_1(\mathbf{R}+\mathbf{t_1}+\mathbf{t_2}) & \quad \beta u_{4x}w_1(\mathbf{R}+\mathbf{t_1}) \\
& u_{4z}v_2(\mathbf{R}+\mathbf{t_1}-\mathbf{t_3}) & \alpha u_{4x}v_2(\mathbf{R}+\mathbf{t_1}) & \quad -\alpha u_{4y}v_2(\mathbf{R}+\mathbf{t_1}+\mathbf{t_2}-\mathbf{t_3}) \\
& & \beta u_{4x}w_2(\mathbf{R}+\mathbf{t_1}) & \quad \beta u_{4y}w_2(\mathbf{R}+\mathbf{t_1}+\mathbf{t_2}-\mathbf{t_3}) \\
& \big(u_{1z}v_1(\mathbf{R}+\mathbf{t_2}) & -\alpha u_{1x}v_1(\mathbf{R}+\mathbf{t_1}) & \quad -\alpha u_{1y}v_1(\mathbf{R}+\mathbf{t_1}+\mathbf{t_2}-\mathbf{t_3}) \\
& & -\beta u_{1x}w_1(\mathbf{R}+\mathbf{t_1}) & \quad \beta u_{1y}w_1(\mathbf{R}+\mathbf{t_1}+\mathbf{t_2}-\mathbf{t_3}) \\
& u_{1z}v_2(\mathbf{R}+\mathbf{t_2}-\mathbf{t_3}) & -\alpha u_{1y}v_2(\mathbf{R}+\mathbf{t_1}-\mathbf{t_3}) & \quad -\alpha u_{1x}v_2(\mathbf{R}) \\
& & \beta u_{1y}w_2(\mathbf{R}+\mathbf{t_1}-\mathbf{t_3}) & \quad -\beta u_{1x}w_2(\mathbf{R}) \\
& u_{2z}v_1(\mathbf{R}+\mathbf{t_1}) & \alpha u_{2y}v_1(\mathbf{R}+\mathbf{t_1}+\mathbf{t_2}) & \quad \alpha u_{2x}v_1(\mathbf{R}+\mathbf{t_2}) \\
& & -\beta u_{2y}w_1(\mathbf{R}+\mathbf{t_1}+\mathbf{t_2}) & \quad \beta u_{2x}w_1(\mathbf{R}+\mathbf{t_2}) \\
& u_{2z}v_2(\mathbf{R}+\mathbf{t_1}) & \alpha u_{2x}v_2(\mathbf{R}) & \quad \alpha u_{2y}v_2(\mathbf{R}+\mathbf{t_2}) \\
& & \beta u_{2x}w_2(\mathbf{R}) & \quad -\beta u_{2y}w_2(\mathbf{R}+\mathbf{t_2}) \\
& -u_{3z}v_1(\mathbf{R}+\mathbf{t_1}+\mathbf{t_2}-\mathbf{t_3}) & \alpha u_{3x}v_1(\mathbf{R}+\mathbf{t_1}+\mathbf{t_2}) & \quad -\alpha u_{3y}v_1(\mathbf{R}+\mathbf{t_2}) \\
& & \beta u_{3x}w_1(\mathbf{R}+\mathbf{t_1}+\mathbf{t_2}) & \quad \beta u_{3y}w_1(\mathbf{R}+\mathbf{t_2}) \\
& -u_{3z}v_2(\mathbf{R}+\mathbf{t_2}-\mathbf{t_3}) & -\alpha u_{3y}v_2(\mathbf{R}+\mathbf{t_2}) & \quad \alpha u_{3x}v_2(\mathbf{R}+\mathbf{t_1}+\mathbf{t_2}-\mathbf{t_3}) \\
& & \beta u_{3y}w_2(\mathbf{R}+\mathbf{t_2}) & \quad \beta u_{3x}w_2(\mathbf{R}+\mathbf{t_1}+\mathbf{t_2}-\mathbf{t_3}) \\
& -u_{4z}v_1(\mathbf{R}+\mathbf{t_1}+\mathbf{t_2}) & \alpha u_{4y}v_1(\mathbf{R}+\mathbf{t_1}) & \quad -\alpha u_{4x}v_1(\mathbf{R}+\mathbf{t_1}+\mathbf{t_2}-\mathbf{t_3}) \\
& & -\beta u_{4y}w_1(\mathbf{R}+\mathbf{t_1}) & \quad -\beta u_{4x}w_1(\mathbf{R}+\mathbf{t_1}+\mathbf{t_2}-\mathbf{t_3}) \\
& -u_{4z}v_2(\mathbf{R}+\mathbf{t_1}) & -\alpha u_{4x}v_2(\mathbf{R}+\mathbf{t_1}+\mathbf{t_2}-\mathbf{t_3}) & \quad \alpha u_{4y}v_2(\mathbf{R}+\mathbf{t_1}-\mathbf{t_3}) \\
& & -\beta u_{4x}w_2(\mathbf{R}+\mathbf{t_1}+\mathbf{t_2}-\mathbf{t_3}) & \quad -\beta u_{4y}w_2(\mathbf{R}+\mathbf{t_1}-\mathbf{t_3}))\Big)
\end{aligned}
$$

$$
\begin{aligned}
C_{3zw2}\Big(& u_{1z}w_1(\mathbf{R}+\mathbf{t_1}) && -\alpha u_{1x}w_1(\mathbf{R}+\mathbf{t_1}+\mathbf{t_2}-\mathbf{t_3}) && -\alpha u_{1y}w_1(\mathbf{R}+\mathbf{t_2}) \\
& && \beta u_{1x}v_1(\mathbf{R}+\mathbf{t_1}+\mathbf{t_2}-\mathbf{t_3}) && -\beta u_{1y}v_1(\mathbf{R}+\mathbf{t_2}) \\
& -u_{1z}w_2(\mathbf{R}+\mathbf{t_1}-\mathbf{t_3}) && \alpha u_{1y}w_2(\mathbf{R}) && \alpha u_{1x}w_2(\mathbf{R}+\mathbf{t_2}-\mathbf{t_3}) \\
& && \beta u_{1y}v_2(\mathbf{R}) && -\beta u_{1x}v_2(\mathbf{R}+\mathbf{t_2}-\mathbf{t_3}) \\
& u_{2z}w_1(\mathbf{R}+\mathbf{t_2}) && \alpha u_{2y}w_1(\mathbf{R}+\mathbf{t_1}) && \alpha u_{2x}w_1(\mathbf{R}+\mathbf{t_1}+\mathbf{t_2}) \\
& && \beta u_{2y}v_1(\mathbf{R}+\mathbf{t_1}) && -\beta u_{2x}v_1(\mathbf{R}+\mathbf{t_1}+\mathbf{t_2}) \\
& -u_{2z}w_2(\mathbf{R}+\mathbf{t_2}) && -\alpha u_{2x}w_2(\mathbf{R}+\mathbf{t_1}) && -\alpha u_{2y}w_2(\mathbf{R}) \\
& && \beta u_{2x}v_2(\mathbf{R}+\mathbf{t_1}) && -\beta u_{2y}v_2(\mathbf{R}) \\
& -u_{3z}w_1(\mathbf{R}+\mathbf{t_1}+\mathbf{t_2}) && \alpha u_{3x}w_1(\mathbf{R}+\mathbf{t_2}) && -\alpha u_{3y}w_1(\mathbf{R}+\mathbf{t_1}+\mathbf{t_2}-\mathbf{t_3}) \\
& && -\beta u_{3x}v_1(\mathbf{R}+\mathbf{t_2}) && -\beta u_{3y}v_1(\mathbf{R}+\mathbf{t_1}+\mathbf{t_2}-\mathbf{t_3}) \\
& u_{3z}w_2(\mathbf{R}+\mathbf{t_2}) && \alpha u_{3y}w_2(\mathbf{R}+\mathbf{t_1}+\mathbf{t_2}-\mathbf{t_3}) && -\alpha u_{3x}w_2(\mathbf{R}+\mathbf{t_2}-\mathbf{t_3}) \\
& && \beta u_{3y}v_2(\mathbf{R}+\mathbf{t_1}+\mathbf{t_2}-\mathbf{t_3}) && \beta u_{3x}v_2(\mathbf{R}+\mathbf{t_2}-\mathbf{t_3}) \\
& -u_{4z}w_1(\mathbf{R}+\mathbf{t_1}+\mathbf{t_2}-\mathbf{t_3}) && \alpha u_{4y}w_1(\mathbf{R}+\mathbf{t_1}+\mathbf{t_2}) && -\alpha u_{4x}w_1(\mathbf{R}+\mathbf{t_1}) \\
& && \beta u_{4y}v_1(\mathbf{R}+\mathbf{t_1}+\mathbf{t_2}) && \beta u_{4x}v_1(\mathbf{R}+\mathbf{t_1}) \\
& u_{4z}w_2(\mathbf{R}+\mathbf{t_1}-\mathbf{t_3}) && \alpha u_{4x}w_2(\mathbf{R}+\mathbf{t_1}) && -\alpha u_{4y}w_2(\mathbf{R}+\mathbf{t_1}+\mathbf{t_2}-\mathbf{t_3}) \\
& && -\beta u_{4x}v_2(\mathbf{R}+\mathbf{t_1}) && -\beta u_{4y}v_2(\mathbf{R}+\mathbf{t_1}+\mathbf{t_2}-\mathbf{t_3}) \\
& -\big(u_{1z}w_1(\mathbf{R}+\mathbf{t_2}) && -\alpha u_{1x}w_1(\mathbf{R}+\mathbf{t_1}) && -\alpha u_{1y}w_1(\mathbf{R}+\mathbf{t_1}+\mathbf{t_2}-\mathbf{t_3}) \\
& && \beta u_{1x}v_1(\mathbf{R}+\mathbf{t_1}) && -\beta u_{1y}v_1(\mathbf{R}+\mathbf{t_1}+\mathbf{t_2}-\mathbf{t_3}) \\
& -u_{1z}w_2(\mathbf{R}+\mathbf{t_2}-\mathbf{t_3}) && \alpha u_{1y}w_2(\mathbf{R}+\mathbf{t_1}-\mathbf{t_3}) && \alpha u_{1x}w_2(\mathbf{R}) \\
& && \beta u_{1y}v_2(\mathbf{R}+\mathbf{t_1}-\mathbf{t_3}) && -\beta u_{1x}v_2(\mathbf{R}) \\
& u_{2z}w_1(\mathbf{R}+\mathbf{t_1}) && \alpha u_{2y}w_1(\mathbf{R}+\mathbf{t_1}+\mathbf{t_2}) && \alpha u_{2x}w_1(\mathbf{R}+\mathbf{t_2}) \\
& && \beta u_{2y}v_1(\mathbf{R}+\mathbf{t_1}+\mathbf{t_2}) && -\beta u_{2x}v_1(\mathbf{R}+\mathbf{t_2}) \\
& -u_{2z}w_2(\mathbf{R}+\mathbf{t_1}) && -\alpha u_{2x}w_2(\mathbf{R}) && -\alpha u_{2y}w_2(\mathbf{R}+\mathbf{t_2}) \\
& && \beta u_{2x}v_2(\mathbf{R}) && -\beta u_{2y}v_2(\mathbf{R}+\mathbf{t_2}) \\
& -u_{3z}w_1(\mathbf{R}+\mathbf{t_1}+\mathbf{t_2}-\mathbf{t_3}) && \alpha u_{3x}w_1(\mathbf{R}+\mathbf{t_1}+\mathbf{t_2}) && -\alpha u_{3y}w_1(\mathbf{R}+\mathbf{t_2}) \\
& && -\beta u_{3x}v_1(\mathbf{R}+\mathbf{t_1}+\mathbf{t_2}) && -\beta u_{3y}v_1(\mathbf{R}+\mathbf{t_2}) \\
& u_{3z}w_2(\mathbf{R}+\mathbf{t_2}-\mathbf{t_3}) && \alpha u_{3y}w_2(\mathbf{R}+\mathbf{t_2}) && -\alpha u_{3x}w_2(\mathbf{R}+\mathbf{t_1}+\mathbf{t_2}-\mathbf{t_3}) \\
& && \beta u_{3y}v_2(\mathbf{R}+\mathbf{t_2}) && \beta u_{3x}v_2(\mathbf{R}+\mathbf{t_1}+\mathbf{t_2}-\mathbf{t_3}) \\
& -u_{4z}w_1(\mathbf{R}+\mathbf{t_1}+\mathbf{t_2}) && \alpha u_{4y}w_1(\mathbf{R}+\mathbf{t_1}) && -\alpha u_{4x}w_1(\mathbf{R}+\mathbf{t_1}+\mathbf{t_2}-\mathbf{t_3}) \\
& && \beta u_{4y}v_1(\mathbf{R}+\mathbf{t_1}) && \beta u_{4x}v_1(\mathbf{R}+\mathbf{t_1}+\mathbf{t_2}-\mathbf{t_3}) \\
& u_{4z}w_2(\mathbf{R}+\mathbf{t_1}) && \alpha u_{4x}w_2(\mathbf{R}+\mathbf{t_1}+\mathbf{t_2}-\mathbf{t_3}) && -\alpha u_{4y}w_2(\mathbf{R}+\mathbf{t_1}-\mathbf{t_3}) \\
& && -\beta u_{4x}v_2(\mathbf{R}+\mathbf{t_1}+\mathbf{t_2}-\mathbf{t_3}) && -\beta u_{4y}v_2(\mathbf{R}+\mathbf{t_1}-\mathbf{t_3})\big)\Big)
\end{aligned}
$$

References

[1] S. Baroni, S. de Gironcoli, A. dal Corso, and P. Giannozzi, Rev. Mod. Phys. **73**, 515 (2001).

[2] M. C. Payne, M. P. Teter, D. C. Allan, T. A. Arias, and J. D. Joannopoulos, Rev. Mod. Phys. **64**, 1045 (1992).

[3] C. J. Fennie and K. M. Rabe, Phys. Rev. Lett. **97**, 267602 (2006).

[4] W. Zhong, D. Vanderbilt, and K. M. Rabe, Phys. Rev. Lett. **73**, 1861 (1994).

[5] W. Zhong, D. Vanderbilt, and K. M. Rabe, Phys. Rev. B. **52**, 6301 (1995).

[6] W. Zhong, D., and Vanderbilt, Phys. Rev. Lett. **74**, 2487 (1995).

[7] U. V. Waghmare and K. M. Rabe, Phys. Rev. B. **55**, 6161 (1997).

[8] I. A. Kornev, S. Lisenkov, R. Haumont, B. Dkhil, and L. Bellaiche, Phys. Rev. Lett. **99**, 227602 (2007).

[9] I. A. Kornev and L. Bellaiche, Phys. Rev. B. **79**, 100105 (2009).

[10] R. E. Cohen, Nature **358**, 136 (1992).

[11] R. Moessner and A. P. Ramirez, Physics Today **59**, 24 (2006).

[12] R. Moessner and J. T. Chalker, Phys. Rev. B. **58**, 12049 (1998).

[13] M. Dawber, K. M. Rabe, and J. F. Scott, Rev. Mod. Phys. **77**, 1083 (2005).

[14] C.-J. Eklund, C. J. Fennie, and K. M. Rabe, Phys. Rev. B. **79**, 220101 (2009).

[15] K. E. Sickafus, J. M. Wills, and N. W. Grimes, J. Am. Ceram. Soc. **82**, 3279 (1999).

[16] A. M. Glazer, Acta Cryst. B **28**, 3384 (1972).

[17] A. M. Glazer, Acta Cryst. A **31**, 756 (1975).

[18] H. T. Stokes, E. H. Kisi, D. M. Hatch, and C. J. Howard, Acta Cryst. B **58**, 934 (2002).

[19] M. E. Lines and A. M. Glass, *Principles and Applications of Ferroelectric and Related Materials* (Oxford University Press, 1977).

[20] V. Zelezny, E. Cockayne, J. Petzelt, M. F. Limonov, D. E. Usvyat, V. V. Lemanov, and A. A. Volkov, Phys. Rev. B. **66**, 224303 (2002).

[21] K. Parlinski, Y. Kawazoe, and Y. Waseda, J. Chem. Phys. **114**, 2395 (2001).

[22] X. Wu, Y. Dong, S. Qin, M. Abbas, and Z. Wu, Sol. St. Comm. **136**, 416 (2005).

[23] V. V. Lemanov, A. V. Sotnikov, E. P. Smirnova, M. Weihnacht, and R. Kunze, Sol. St. Comm. **110**, 611 (1999).

[24] R. D. King-Smith and D. Vanderbilt, Phys. Rev. B. **49**, 5828 (1994).

[25] E. Cockayne and B. P. Burton, Phys. Rev. B. **62**, 3735 (2000).

[26] W. Zhong and D. Vanderbilt, Phys. Rev. Lett. **74**, 2587 (1995).

[27] N. Sai and D. Vanderbilt, Phys. Rev. B. **62**, 13942 (2000).

[28] S. M. Nakhmanson, K. M. Rabe, and D. Vanderbilt, Phys. Rev. B. **73**, 060101 (2006).

[29] S. M. Nakhmanson, K. M. Rabe, and D. Vanderbilt, Appl. Phys. Lett. **87**, 102906 (2005).

[30] A. Zayak, S. Nakhmanson, and K. M. Rabe, *2006 Workshop on Fundamental Physics of Ferroelectrics*, `http://people.gl.ciw.edu/cohen/meetings/ferro2006/ProgramFerro06_final.pdf`.

[31] N. A. Pertsev, A. K. Tagantsev, and N. Setter, Phys. Rev. B. **61**, 825 (2000).

[32] A. Antons, J. B. Neaton, K. M. Rabe, and D. Vanderbilt, Phys. Rev. B. **71**, 024102 (2005).

[33] A. Vasudevarao, A. Kumar, L. Tian, J. H. Haeni, Y. L. Li, C.-J. Eklund, Q. X. Jia, R. Uecker, P. Reiche, K. M. Rabe, et al., Phys. Rev. Lett. **97**, 257602 (2006).

[34] J. H. Haeni, P. Irvin, W. Chang, R. Uecker, P. Reiche, Y. L. Li, S. Choudhury, W. Tian, M. E. Hawley, B. Craigo, et al., Nature (London) **430**, 758 (2004).

[35] P. E. Blöchl, Phys. Rev. B. **50**, 17953 (1994).

[36] G. Kresse and D. Joubert, Phys. Rev. B. **59**, 1758 (1999).

[37] G. Kresse and J. Hafner, Phys. Rev. B. **47**, 558 (1993).

[38] G. Kresse and J. Furthmüller, Phys. Rev. B. **54**, 11169 (1996).

[39] R. D. King-Smith and D. Vanderbilt, Phys. Rev. B. **47**, 1651 (1993).

[40] W. Zhong, R. D. King-Smith, and D. Vanderbilt, Phys. Rev. Lett. **72**, 3618 (1994).

[41] R. D. King-Smith and D. Vanderbilt, Phys. Rev. B. **49**, 5828 (1994).

[42] O. Dieguez, K. M. Rabe, and D. Vanderbilt, Phys. Rev. B. **72**, 144101 (2005).

[43] H. T. Stokes, D. M. Hatch, and B. J. Campbell, *Isotropy*, `http://stokes.byu.edu/isotropy.html` (2007).

[44] A. T. Zayak, X. Huang, J. B. Neaton, and K. M. Rabe, Phys. Rev. B. **74**, 094104 (2006).

[45] H. T. Stokes and D. M. Hatch, *Findsym*, `http://stokes.byu.edu/isotropy.html` (2004).

[46] D. I. Bilc and D. J. Singh, Phys. Rev. Lett. **96**, 147602 (2006).

[47] M. A. Subramanian, G. Aravamudan, and G. V. S. Rao, Prog. Solid State Chem. **15**, 55 (1983).

[48] O. Tchernyshyov, R. Moessner, and S. L. Sondhi, Phys. Rev. B. **66**, 064403 (2002).

[49] S.-H. Lee, G. Gasparovic, C. Broholm, M. Matsuda, J.-H. Chung, Y. J. Kim, H. Ueda, G. Xu, P. Zschack, K. Kakurai, et al., J. Phys. Cond. Matt. **19**, 145259 (2007).

[50] S. Ji, S.-H. Lee, C. Broholm, T. Y. Koo, W. Ratcliff, S.-W. Cheong, and P. Zschack, Phys. Rev. Lett. **103**, 037201 (2009).

[51] S.-H. Lee, C. Broholm, T. H. Kim, W. R. II, and S.-W. Cheong, Phys. Rev. Lett. **84**, 3718 (2000).

[52] J.-H. Chung, M. Matsuda, S.-H. Lee, K. Kakurai, H. Ueda, T. J. Sato, H. Takagi, K.-P. Hong, and S. Park, Phys. Rev. Lett. **95**, 247204 (2005).

[53] V. N. Glazkov, A. M. Farutin, V. Tsurkan, H.-A. K. von Nidda, and A. Loidl, Phys. Rev. B. **79**, 024431 (2009).

[54] C. J. Fennie and K. M. Rabe, Phys. Rev. Lett. **96**, 205505 (2006).

[55] G.-W. Chern, C. J. Fennie, and O. Tchernyshyov, Phys. Rev. B. **74**, 060405 (2006).

[56] K. T. Chan, J. D. Sau, P. Zhang, and M. L. Cohen, Phys. Rev. B. **75**, 054304 (2007).

[57] A. N. Yaresko, Phys. Rev. B. **77**, 115106 (2008).

[58] N. Metropolis, A. W. Rosenbluth, M. N. Rosenbluth, and A. H. Teller, J. Chem. Phys. **21**, 1087 (1953).

Curriculum Vitae

Carl-Johan Eklund

Education

2010 Ph.D., Rutgers University

2001 M.Sc., Chalmers University of Technology

1996 Diploma, University of Savoy

Publications

C.-J. Eklund, C. J. Fennie, and K. M. Rabe, Phys. Rev. B **79**, 220101(R) (2009).

P. Entel, M. E. Gruner, W. A. Adeagbo, C.-J. Eklund, A. T. Zayak, H. Akai, and M. Acet, J. Magn. Magn. Mater. **310**, 2761 (2007).

A. Vasudevarao, A. Kumar, L. Tian, J. H. Haeni, Y. L. Li, C.-J. Eklund, Q. X. Jia, R. Uecker, P. Reiche, K. M. Rabe, L. Q. Chen, D. G. Schlom, and V. Gopalan, Phys. Rev. Lett. **97**, 257602 (2006).